ELSEVIER

Contents lists available at ScienceDirect

# **Computer Physics Communications**

journal homepage: www.elsevier.com/locate/cpc



Computational Physics

# Analytic model for the propagation of a collisionless neutral beam



Lynton Appel <sup>10</sup>

UKAEA (United Kingdom Atomic Energy Authority), Culham Campus, Abingdon, Oxfordshire, OX14 3DB, United Kingdom of Great Britain and Northern Ireland

#### ARTICLE INFO

The review of this paper was arranged by Prof David W Walker

Keywords:
Neutral beam
NBI
Probability
Distribution
Magnetic confinement fusion
Bayesian

#### ABSTRACT

This paper introduces an analytical model for the propagation of collisionless neutral particles in neutral beam injection (NBI) systems. The model incorporates a novel approach using composite Gaussian basis functions to represent non-Gaussian source distributions and extends to two-dimensional source configurations under orthogonal separability assumptions. The method efficiently computes particle velocity and spatial distributions along beam trajectories, accounting for truncation effects due to transmission losses. The model has been implemented as a computational module in the Minerva framework and interfaced with the ITER Integrated Modelling & Analysis Suite (IMAS).

A case study of the MAST Upgrade NBI system demonstrates the model's ability to predict particle distributions from the source grid to the plasma cavity while accommodating detailed baffle geometries and calculating transmission factors. Comparisons reveal that reduced Gaussian basis representations can achieve an order-of-magnitude reduction in computational time with negligible impact on accuracy. The proposed model provides a fast and rigorous alternative to Monte Carlo simulations, enabling enhanced diagnostic modelling and efficient integration with Bayesian inference frameworks.

#### 1. Introduction

High-energy neutral beam systems play a vital role in the current generation of tokamak and stellarator magnetic confinement devices, serving both as a key mechanism for plasma heating and current drive [1] and as a valuable diagnostic tool for plasma quantities [2,3]. In this paper we consider the propagation of a collisionless particle beam distribution as a precursor to its modification by collisions with populations of neutrals and ions. Here the challenge lies in achieving a fast and accurate analysis involving integrals over 6-dimensional phase space (i.e. three spatial and three in velocity) whilst simultaneously including details of a realistic geometrical configuration.

High accuracy codes generally use Monte-Carlo techniques to evolve trajectories of individual particles, for example FREYA [4], NFREYA [5], TRANSP [6], NUBEAM [7], MSESIM [8], BBNBI [9] and FIDASIM [10]. These codes couple the collisionless treatment of the high energy neutrals with collisional models of the beam deposition in the plasma cavity. The most significant issue with these codes is that execution time tends to be long as a large number of particles need to be followed to reduce statistical fluctuations. However, through simplifications in the beam formulation, codes such as PENCIL [11] and SUPERCODE [12] are capable of generating faster approximating solutions. The SINBAD code [13] offers improvements over these earlier first-generation approximate methods. Based on a so-called *narrow beam model* the ap-

proach in SINBAD assumes the beam source is planar with a small cross-sectional area compared to the length of the beam-line. Results from SINBAD provide reasonable matches to FREYA, TRANSP and to measured NBI data [13]. The NEMO code [14] is a modernised version of the SINBAD code enabling it to be included in the CRONOS integrated modelling suite [15] and to be used by the European Integrated Tokamak Modelling Task Force (ITM-TF) [16]. The NEBULA code [17] also uses the *narrow beam model* proposed by SINBAD. A similar but not identical approach has been recently described by Bannmann *et al.* [18,19] to model neutral beam injection and halo formation using a set of Gaussian pencil (Gausscil) beams, formed by dividing the source grid into a set of rectangular areas. The results of the model are shown to be in good agreement with FIDASIM.

Whilst earlier approaches (for example PENCIL) treated the beam as a single entity, later models provided the capability of sub-dividing the beam and summing the contributions; it was found that the number of subdivided beams required is less than the total number of Positive Ion Neutral Injector (PINI) beamlets and as low as 2x5 [18] which is an advantage for computational speed. The main hypothesis for the application of these simplified approaches is that the plasma conditions are sufficiently homogeneous across the constituent beamlets in planes parallel to the beam source; this sets a condition on the minimum number of beamlets and ultimately limits the applicability for using a non Monte-Carlo method.

E-mail address: lynton.appel@ukaea.uk.

https://doi.org/10.1016/j.cpc.2025.109610

Received 8 July 2024; Received in revised form 12 March 2025; Accepted 3 April 2025

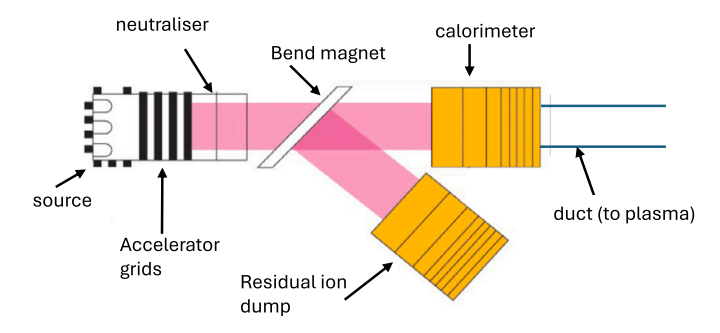


**Fig. 1.** Schematic of the neutral beam system on MAST Upgrade illustrating the salient features of a generic system. (figure is based on [20]).

Fig. 1 shows a schematic of the beam system on MAST Upgrade. The first stage is the generation of ions. These are subsequently accelerated, shaped and focussed via an electric field generated by a cascade of grids held at fixed potentials. The final grid is at *tokamak (or device)* earth potential and particles emerge into a neutralisation chamber. Following this, remaining ions are diverted off to a beam dump with an applied magnetic field, whilst the neutral particles stream down a duct into the plasma (tokamak or stellarator) cavity. During the final transit a proportion of the neutral particles may be reionised due to interactions with the background neutral gas. Furthermore, the presence of baffles or other fixed components may scrape off part of the streaming neutral particle beam; these are collectively referred to as *transmission losses*.

The usual approach for computing the neutral beam distribution arriving into the plasma cavity is to start with the flux of fast ions exiting the final earthed acceleration grid into the neutraliser chamber. The salient features relevant for determining the downstream beam distribution are as follows:

- 1. The velocity distribution of the neutralised ions in the neutraliser chamber matches the distribution of the source ions exiting the final accelerator grid. Evidence to support this is contained in a recently published computational model for space charge neutralisation of positive ion beams, Holmes and McAdams [21] who show that for a Deuterium beam of 120 kV, 60 A the role of space charge forces is inconsequential in the beam transport at least until the bend magnet is reached. Similar evidence is available for ITER negative ion beams from simulations using the OPERA code [22].
- 2. The neutraliser efficiency is known. The overall neutraliser efficiency is generally obtained by a combination of measurements taken within the beamline during dedicated calibration exercises and simulation [23–25]. Typical values on JET for deuterium injection range from 30-60% depending on precise details of beam species mix produced by the ion source and acceleration voltage.
- 3. The transmission factor is known. The beam transmission factor accounts for "baffle losses": particles lost by interactions with structures at the edge of the beam. The transmission factor cannot be obtained by direct measurement and thus is estimated. On JET, this is achieved by combining neutral beam test bed data with ray tracing simulations giving a value of 75% [25]. This factor therefore accounts for one of the largest uncertainties in the overall beam power delivered to the plasma which, combined with other uncertainties results in a total uncertainty of 10% in power delivered to JET. The PINI simulator code [26] takes full account of baffle losses as do other codes, for example BBNBI which has been used to model JET and AUG tokamaks [9]. Another factor included in the PINI simulator code is transmission losses due to reionisation of the beam with the background gas in the duct between the neutraliser chamber and the tokamak plasma cavity.
- 4. Spatial variations in the beam flux and velocity divergence on the beam source grid are known. For the JET PINI ion source design, detailed measurements of the ion-source non-uniformity were made on the

NB test-bed(NBTB) [27–29]. Measurements of the beam profile with high spatial resolution and accurate electrical measurements at the PINI accelerator grids were then combined with detailed modelling to infer the beam divergence characteristics. For each JET PINI, following initial construction and again after any significant engineering work on the PINI, a detailed characterisation exercise was executed on the NBTB recording the beam profile over a wide range of voltages and perveance values. (These characterisations are kept as internal reports and are not generally available to the public). Lacking dedicated test-bed measurements as is the case for JET PINIs, the MAST Upgrade beams rely on the fact that the construction of its PINIs is very similar to the JET PINIs.

In this paper we describe a new analytical approach to calculate the propagation of a probability density function (PDF) of collisionless neutral particles with a Maxwellian velocity distribution and arbitrary spatial distribution emitted from a surface towards a fixed focus. In comparison with previous approaches based on the narrow beam model of SINBAD or the Gaussian pencil beams of Bannmann, the methodology presented in this paper is mathematically rigorous relating the PDF at the source with the PDF at any point beyond the source. This is achieved by a change of variables enabling a 1:1 mapping of particles between the source and points beyond. The model takes into account transmission losses, expressed as a truncation in the velocity component of the PDF. An outcome of the model is that the PDF at any point both on the source or elsewhere can be expressed as the product of two PDFs for the spatial and velocity distributions. Furthermore, contrary to the assumption of constant velocity variance employed in other simplified models, the velocity variance changes with distance from the source.

Section 2 considers the case of a spatially truncated 1-D source with normal distribution, and with a normally distributed angular velocity (pitch). Expressions for the full distribution at a fixed normal distance from the source are expressed as the product of two constituent distributions in pitch and in spatial position. Sections 3 compares results from the new analytic model with the model used in [18] and from 1-D ray-tracing calculations. Section 4 includes the effects of baffle losses on the particle distribution and obtains the transmission factor. Section 5 considers non-Gaussian source distributions. This is accomplished by expressing the distribution in terms of a set of overlapping Gaussian distributions whose magnitude are computed such that on aggregate they match the source distribution. Section 6 extends the model to a 2-D source distribution. Finally section 7 presents results of the model applied to the MAST Upgrade tokamak.

## 2. 1-D source distribution

This section derives an analytical expression for the particle distribution at an arbitrary point ahead of a distributed particle source. Fig. 2 illustrates the geometry, aligned with the right-handed Cartesian coordinates u,v,w and unit vectors  $\underline{\hat{u}}$ ,  $\underline{\hat{v}}$ ,  $\underline{\hat{w}}$ . The particle source lies on the vertical line through points O and Q extending from  $q_{min}$  to  $q_{max}$  with peak density at O and is directed towards a focal point F. The dashed-dotted line through O and F represents the locus of peak density. While most of the beam is constrained within the dashed lines, velocity divergence causes some particles to deviate beyond these boundaries. Point P is situated on line X-X, parallel to the source. The mapping  $Q \to P$  represents particles with pitch angle  $\theta$  emitted from Q and arriving at P on line X-X.

The positions of points P, Q and F are defined as follows:

$$P = O + p_u \hat{\underline{u}} + p_v \hat{\underline{v}} \tag{1}$$

$$Q = O + q\underline{\hat{v}} \tag{2}$$

$$F = O + f_u \hat{u} + f_v \hat{v} \tag{3}$$

$$\cos \theta_{\mu} = \frac{F - Q}{|FQ|} \cdot \hat{\underline{u}} \tag{12}$$

Combining these relations, we find:

$$(P - Q) \cdot \hat{u} \tan \theta = (P - Q) \cdot \hat{v} \tag{13}$$

$$(F - Q) \cdot \underline{\hat{u}} \tan \theta_{u} = (F - Q) \cdot \underline{\hat{v}}$$
(14)

Substituting equations (1), (2) and (3) for P, Q and F respectively

$$q = -p_u \tan \theta + p_v \tag{15}$$

$$\tan \theta_{\mu} = \frac{f_v - q}{f_{\mu}} \tag{16}$$

In the limit  $f_u \gg f_v - q$ , the small-angle approximation  $\tan \theta_u \sim \theta_u$ holds. Furthermore equation (4) indicates that significant values of  $g(q, \theta, \theta_u)$  occur when  $(\theta - \theta_u)/\delta \sim 1$ , implying  $\theta \sim \delta + \theta_u$  if  $\delta \ll 1$ . Combining these approximations yields  $\tan \theta \sim \theta$ . These approximations are satisfied in the JET and ITER neutral beamlines [30,31]. Under these conditions, equations (15) and (16) simplify to:

$$q = -p_u \theta + p_v \tag{17}$$

$$\theta_{\mu} = \frac{f_{\nu} - q}{f_{\mu}} \tag{18}$$

Rearranging these equations yields:

$$\theta = \frac{p_v - q}{p_u} \tag{19}$$

$$\theta_{\mu} = \frac{p_{\mu}\theta - p_{\nu} + f_{\nu}}{f_{\nu}} \tag{20}$$

The following section uses these small-angle approximations as expressed in equations (17) to (20).

# $(a = a_{\min})$

Fig. 2. Configuration of problem with a 1-D source. The point B is a single baffle point creating an obstruction (see section 4).

The PDF of particles at the source based on position q and pitch angle

$$g(q,\theta) = \begin{cases} \frac{A}{n_2} \exp\left(-\frac{q^2}{2\sigma^2} - \frac{(\theta - \theta_{\mu})^2}{2\delta^2}\right) \\ \text{if } q_{\min} \le q \le q_{\max} \text{ and } -\frac{\pi}{2} \le \theta \le \frac{\pi}{2} \\ 0 \text{ otherwise} \end{cases}$$
 (4)

where  $\theta_{\mu}$  denotes the counter-clockwise angle between the normal to the source  $(\hat{u})$  and  $\overline{QF}$ , while  $\theta$  is the counter-clockwise angle between  $\hat{u}$  and  $\overline{QP}$ . The normalisation constant A and the terms  $n_1$ ,  $n_2$  are given

$$A = \frac{1}{2\pi\sigma\delta n_1} \tag{5}$$

$$n_1 = \Phi\left(\frac{q_{max}}{\sigma}\right) - \Phi\left(\frac{q_{min}}{\sigma}\right) \tag{6}$$

$$n_2 = \Phi\left(\frac{\pi/2 - \theta_{\mu}}{\delta}\right) - \Phi\left(\frac{-\pi/2 - \theta_{\mu}}{\delta}\right) \tag{7}$$

where  $\Phi(x)$  is the cumulative distribution function (CDF) of the standard normal distribution:

$$\Phi(x) = \frac{1}{2} \left( 1 + \operatorname{erf}(x/\sqrt{2}) \right) \tag{8}$$

with  $erf(\cdot)$  denoting the error function.

The PDF  $g(q, \theta)$  characterises the source distribution as a spatially truncated normal distribution centred about the point O and truncated normal velocity distribution directed towards focus F. In the next section we derive expressions to map this distribution to the line X-X which is parallel to the source and located a distance  $p_u$  from it, i.e.  $g(q,\theta) \rightarrow g_{\alpha}(p_v,\theta)$ . To facilitate this mapping, we derive expressions relating the coordinates and angles involved. By computing the scalar and cross products of vectors  $\overline{FQ}$  and  $\overline{PQ}$  with  $\hat{u}$  we obtain:

$$\sin\theta = \frac{P - Q}{|PO|} \cdot \hat{\underline{p}} \tag{9}$$

$$\cos\theta = \frac{P - Q}{|PO|} \cdot \hat{\underline{u}} \tag{10}$$

$$\sin \theta_{\mu} = \frac{F - Q}{|FQ|} \cdot \hat{\underline{p}} \tag{11}$$

## 2.1. Transformation of PDF

In this section we obtain the mapping  $g(q,\theta) \to g_{\alpha}(p_{\nu},\theta)$ , expressed in separable form as the product of two component PDFs:

$$g_{\alpha}(p_{v}, \theta; p_{u}) = g_{1}(\theta; p_{u}, p_{v})g_{2}(p_{v}; p_{u})$$
(21)

where the notation a, b; c indicates that a PDF is a function of variables  $\{a,b\}$  and c is an additional parameter (i.e.  $\int g_x(a,b;c)da\,db=1$ ). Whereas  $g_{\alpha}$  describes the total mapped PDF in an arbitrary position in phase space, the components  $g_1$  and  $g_2$  each express distinct aspects of  $g_{\alpha}$ . The PDF  $g_1$  is the velocity distribution at a single spatial point  $(p_u, p_v)$  and the PDF  $g_2$  is the spatial distribution evaluated on the section X - X located at  $p_u$  shown in Fig. 2. Substituting equations (17) and (20) into (4) to eliminate q and  $\theta_{\mu}$ , the PDF  $g_{\alpha}$  defined in equation (21) can be expressed as:

$$g_{\alpha}(p_{\nu},\theta;p_{\mu}) = AJ \exp(-a\theta^2 - b\theta - c)$$
 (22)

$$a = \frac{p_u^2 f_u^2 \delta^2 + \sigma^2 (f_u - p_u)^2}{2\sigma^2 f_u^2 \delta^2}$$
 (23)

$$b = -\frac{p_u p_v f_u^2 \delta^2 + \sigma^2 (p_u - f_u)(p_v - f_v)}{\sigma^2 f_u^2 \delta^2}$$
 (24)

$$c = \frac{p_v^2 f_u^2 \delta^2 + \sigma^2 (f_v - p_v)^2}{2\sigma^2 f_v^2 \delta^2}$$
 (25)

$$J = \begin{vmatrix} \frac{\partial q}{\partial p_v} \Big|_{\theta} & \frac{\partial q}{\partial \theta} \Big|_{p_v} \\ \frac{\partial \theta}{\partial p_v} \Big|_{\theta} & \frac{\partial \theta}{\partial \theta} \Big|_{p_v} \end{vmatrix} = 1 \tag{26}$$

is the Jacobian determinant accounting for the change of variable from  $\{q,\theta\}$  to  $\{p_n,\theta\}$ . Completing the square for  $\theta$ , equation (22) can be written as a product of two PDF functions as shown in equation (21) with

$$g_{1}(\theta; p_{u}, p_{v}) = \begin{cases} \frac{1}{\sqrt{2\pi}\sigma_{*}n_{2}} \exp\left(-\frac{(\theta - \mu_{*})^{2}}{2\sigma_{*}^{2}}\right) & \theta_{min} \leq \theta \leq \theta_{max} \\ 0 & \theta < \theta_{min} \\ 0 & \theta > \theta_{max} \end{cases}$$
(27)

$$g_2(p_v; p_u) = Bn_2(p_u, p_v) \exp\left(-\frac{(p_v - \mu_r)^2}{2\sigma_r^2}\right)$$
 (28)

$$\mu_*(p_u, p_v) = \frac{-b}{2a} = \frac{hp_v(hp_u - f_u) + hf_v(f_u - p_u)}{k}$$
 (29)

$$\sigma_*(p_u)^2 = \frac{1}{2a} = \frac{f_u^2 \delta^2 h}{k} \tag{30}$$

$$\mu_r(p_u) = \frac{f_v p_u}{f_u} \tag{31}$$

$$\sigma_r^2(p_u) = \sigma^2 \left( \frac{(hp_u - f_u)^2}{hf_u^2} + \frac{h - 1}{h} \right)$$
 (32)

$$\theta_{\min}(p_u, p_v) = \begin{cases} \tan^{-1}\left(\frac{p_v - q_{\max}}{p_u}\right), & p_u > 0\\ -\frac{\pi}{2}, & p_u = 0 \text{ and } q_{\min} < p_v < q_{\max}\\ 0 & \text{otherwise} \end{cases}$$

$$\theta_{\max}(p_u, p_v) = \begin{cases} \tan^{-1}\left(\frac{p_v - q_{\min}}{p_u}\right), & p_u > 0\\ +\frac{\pi}{2}, & p_u = 0 \text{ and } q_{\min} < p_v < q_{\max}\\ 0 & \text{otherwise} \end{cases}$$
(34)

$$n_{2}(p_{u},p_{v}) = \Phi\left(\frac{\theta_{\text{max}} - \mu_{*}}{\sigma_{*}}\right) - \Phi\left(\frac{\theta_{\text{min}} - \mu_{*}}{\sigma_{*}}\right) \tag{35}$$

$$B(p_u) = A\sqrt{2\pi}\sigma_* \tag{36}$$

in which

$$h = 1 + \frac{\delta^2 f_u^2}{\sigma^2} \tag{37}$$

$$k(p_{u}) = (hp_{u} - f_{u})^{2} + (h - 1)f_{u}^{2}$$
(38)

In the limits  $|p_v - q_{min}| \ll p_u$  and  $|p_v - q_{max}| \ll p_u$ , equations (33) and

$$\theta_{min}(p_u, p_v) \approx \frac{p_v - q_{max}}{p_u} \tag{39}$$

$$\theta_{max}(p_u, p_v) \approx \frac{p_v - q_{min}}{p_u} \tag{40}$$

In this limit, substituting for  $\theta_{min},~\theta_{max},~\mu_*,$  the arguments of the  $\Phi(\cdot)$ terms appearing in equation (35) are:

$$\frac{\theta_{min} - \mu_*}{\sigma} = -\frac{h(f_u p_v + f_v p_u)(f_u - p_u) + kq_{max}}{\sigma p_u k}$$
(41)

$$\frac{\theta_{min} - \mu_*}{\sigma_*} = -\frac{h(f_u p_v + f_v p_u)(f_u - p_u) + kq_{max}}{\sigma_* p_u k}$$

$$\frac{\theta_{max} - \mu_*}{\sigma_*} = -\frac{h(f_u p_v + f_v p_u)(f_u - p_u) + kq_{min}}{\sigma_* p_u k}$$
(41)

When  $p_u = f_u$ , these simplify to

$$\frac{\theta_{min} - \mu *}{\sigma_*} \bigg|_{p_u = f_u} = -\frac{q_{max}}{\sigma_* p_u}$$

$$\frac{\theta_{max} - \mu_*}{\sigma_*} \bigg|_{p_u = f_u} = -\frac{q_{min}}{\sigma_* p_u}$$
(43)

$$\left. \frac{\theta_{max} - \mu_*}{\sigma_*} \right|_{p_* = f_*} = -\frac{q_{min}}{\sigma_* p_u} \tag{44}$$

and  $n_2$  is independent of  $p_n$ .

From equations (27) to (44), we observe that by considering a fixed focus  $(f_u, f_v)$ :

- 1.  $g_1(\theta; p_u, p_v)$  is a truncated normal distribution whereas  $g_2(p_v; p_u)$  is a truncated normal distribution at  $p_u = 0$  (this is consistent with equation (4)) and an unbounded distribution for  $p_u > 0$ .
- The parameters of the normal distribution  $g_1(\theta;p_u,p_v)$  are  $\sigma_*$ ,  $\mu_*$ and  $n_2$ . The parameter  $n_2$  expresses the truncation of the normal distribution;  $\sigma_*$  is independent of both  $p_v$  and  $f_v$ , whereas for a given value of  $p_u$ ,  $\mu_*$  varies linearly with  $p_v$ . The characteristics are plotted in Fig. 3.

At specific limits,

- (a) when  $p_u = 0$  (at the source plane),  $\mu_* = (f_v p_v)/f_u$ ,  $\sigma_* = \delta$ (i.e.  $\delta$  is consistent with equation (4)).
- (b) when  $p_u = f_u$  (at the focal plane),  $\mu_* = p_v/f_u$ ,  $\sigma_* = \sigma/f_u$ . (i.e. at longer focal distances the beam becomes more collimated and with a reduced standard deviation in velocity.)
- (c) when  $p_u = f_u/h$ ,  $\mu_* = f_v/f_u$ , i.e.  $\mu_*$  is independent of  $p_v$ ; and  $\sigma_* = \sqrt{\delta^2 + (\sigma/f_u)^2}$ , increasing from  $\sigma_* = \delta$  at  $p_u = 0$ , and thereafter decreasing with  $\sigma_* = 0$  as  $p_u \to \infty$ .
- (d) in the limit  $p_u/f_u \to \infty$ ,  $\mu_* = p_v(1 f_v)$  and  $\sigma_* = 0$  i.e. at distances well beyond the focus, the mean velocity direction varies linearly with  $p_v$  and its variance is zero.
- (e) in the limit  $f_u/p_u \to \infty$ ,  $\mu_* = p_v(hf_v 1)$  and  $\sigma_* = \delta$  i.e. as the focal point moves towards ∞ at finite distances from the source the mean velocity direction varies linearly and its variance is  $\delta^2$ .
- 3. The parameters of  $g_2(p_v; p_u)$  are B,  $n_2$ ,  $\mu_r$  and  $\sigma_r$ . The parameter Bis a normalising factor to ensure that  $\int g_2(p_v; p_u) dp_v = 1$ . Fig. 4(a) plots the variation of  $n_2$ ; at  $p_u = f_u$  the variation in  $n_2$  with respect to  $p_v$  reduces to zero and  $g_2(p_v; p_u)$  is a normal distribution. Fig. 4(b) plots the variation of  $\sigma_r$ . Although  $g_2(p_v; p_u)$  is not in general a Gaussian distribution,  $\sigma_r$  provides an approximation to the standard deviation fit to a normal distribution.

At specific limits,

(33)

- (a) when  $p_{\mu} = 0$  (at the source plane),  $\mu_r = 0$ ,  $\sigma_r = \sigma$  (i.e.  $\sigma_r$  is consistent with equation (4)).
- (b) when  $p_u = f_u$  (at the focal plane),  $\mu_r = f_v$ , and  $\sigma_r = \delta f_u$ . In the limit  $|p_v-q_{min}|\ll p_u$  and  $|p_v-q_{max}|\ll p_u,\ g_2(p_v;p_u)$  is a truncated Gaussian.
- (c) when  $p_u = f_u / h$ ,  $\sigma_r^2 = h \sigma^2 / f_u^2$ ,  $\mu_r = f_v$ .
- (d) in the limit  $p_u/f_u \to \infty$ ,  $\sigma_r = \infty$  and
  - if  $f_v = 0$  then  $\mu_r = 0$
  - if  $f_v > 0$  then  $\mu_r = +\infty$
  - if  $f_v < 0$  then  $\mu_r = -\infty$

i.e. at distances well beyond the focus, the radial variance tends to  $\infty$  whereas its mean value dependence on whether  $f_v$  is nonzero, and also its sign if non-zero.

- (e) in the limit  $f_u/p_u \to \infty$ ,  $\mu_r = 0$  and  $\sigma_r = \sigma$  i.e. as the focal point moves towards ∞ at finite distances from the source the radial variance tends to  $\sigma$  and its mean velocity is zero.
- 4. The  $p_u$ -value where  $\sigma_r$  and  $\sigma_*$  reach their extreme points and where  $\mu_*$  is independent of  $p_v$  are all coincident at  $p_u = f_u/h$ . Since in general h > 1 (see equation (37)) this position always lies between the beam source  $(p_u = 0)$  and the focal plane  $(p_u = f_u)$ .

# 3. Model validation

In this section we compare the results of the 1-D model described in section 2 with a 1-D ray-tracing model and with the Bannmann model for a single Gausscil Beam. The parameters are based on the neutral beam assembly installed on MAST Upgrade [31] that has a beam halfwidth = 82.5 mm, focus = 12 m, and beam divergence of 0.6 degrees. The line joining the mid-point of the source and focal point is taken to be perpendicular to the source. Specific details of the models are as follows:

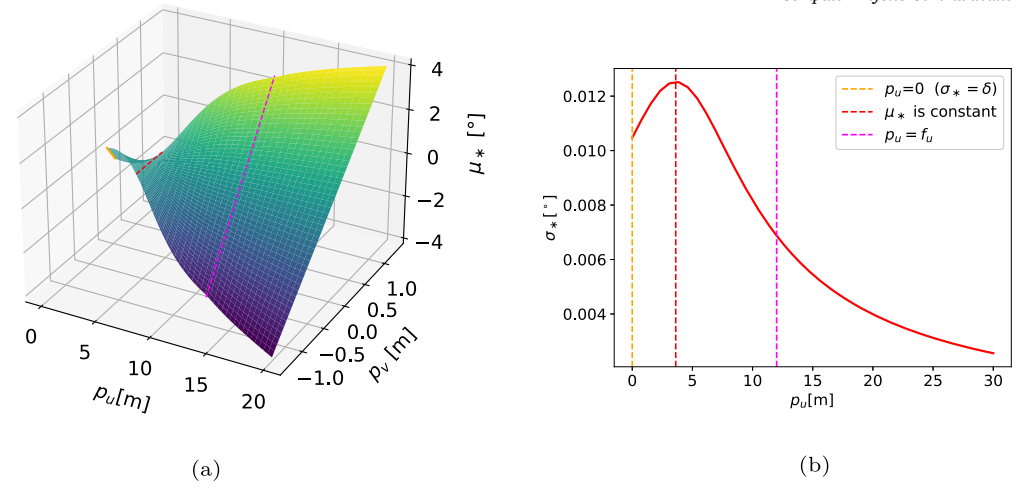


Fig. 3. (a) Variation of  $\mu_*$  with  $p_u$  and  $p_v$ . (b) Variation of  $\sigma_*$  with  $p_u$ . The lines shown are at  $p_u=0$  (orange line) and  $p_u=f_u$  (magenta line). The red line is at the value of  $p_u$  where  $\mu_*$  is independent of  $p_v$ ,  $\sigma_*$  reaches its maximum value and  $\sigma_r$  (see Fig. 4b) reaches it minimum value. (Beam parameters are  $\sigma=82.5$  mm,  $\delta=0.6$  degrees, O=(0,0), F=(12m,0),  $q_{min}=-\sigma$ ,  $q_{max}=+\sigma$ ). (For interpretation of the colours in the figure(s), the reader is referred to the web version of this article.)

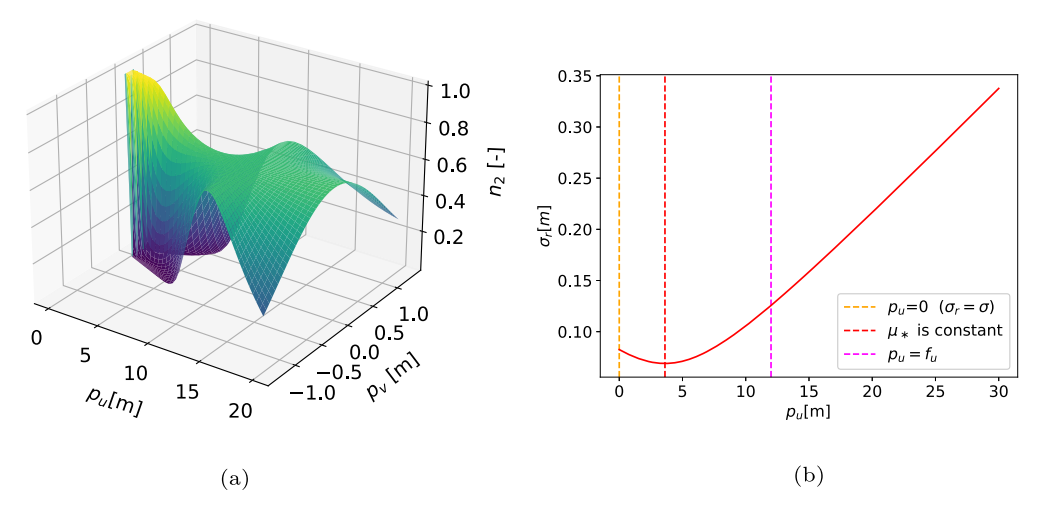


Fig. 4. (a) Variation of  $n_2$  with  $p_u$  and  $p_v$ . (b) Variation of  $\sigma_r$  with  $p_u$ . The lines shown are at  $p_u=0$  (orange line) and  $p_u=f_u$  (magenta line). The red line is at the value of  $p_u$  where both  $\mu_*$  is constant and  $\sigma_*$  reaches its minimum value. (Beam parameters are  $\sigma=82.5$  mm,  $\delta=0.6$  degrees, O=(0,0), F=(12m,0),  $q_{min}=-\sigma$ ,  $q_{max}=+\sigma$ ).

#### Monte-Carlo model

For the purpose of validating the model described in section 2, a 1-D ray tracing code was written in Python. The geometry is as shown in Fig. 2. A set of rays ( $n=10^8$ ), spatially distributed according to a truncated normal distribution about q=0 with standard deviation 82.5 mm were launched from the source within the range  $q_{min} < q < q_{max}$ . The orientation of each ray emanating from a given point was sampled from a normal distribution with a mean orientation directed towards the focal point and with angular standard deviation 0.6 degrees. The rays were projected a distance u from the source, and results presented as histograms.

# Bannmann model

The Bannmann model represents the beam source by a set of Gausscil beams. Fig. 5 illustrates a single Gausscil for the case  $\delta < \gamma$  on orthogonal axes uv. The geometrical details are taken from its implementation in the Minerva Bayesian framework [32]. The beam source, located at u=0 on the left side of the figure, follows a normal distribution  $\mathcal{N}(0,\sigma^2)$  about the point O=(0,0) with  $\sigma=w/2=82.5$  mm, truncated at  $v=\pm\sigma$ . Particles are emitted from all points at the source in the positive u-

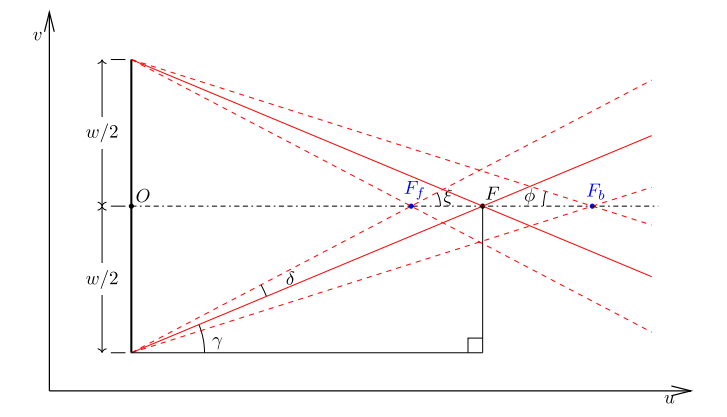


**Fig. 5.** Geometrical depiction of a single Gausscil beam  $(\gamma > \delta)$  [18].

direction towards the focus F with a divergence angle  $\delta$ . The solid lines in the figure show the trajectory of two particles launched with zero divergence from the extreme edges of the source converging at the focal point  $F=(f_u,0)$ . Neglecting velocity divergence, all particles would converge at F. However, velocity divergence causes the majority of par-

ticles launched at the source to miss F. To account for this, the model introduces an ad hoc assumption: particles pass through one of two "virtual" focal points, depending on their observed position. These virtual focal points,  $F_f = (f_f, 0)$  and  $F_b = (f_b, 0)$ , are defined by the trajectories of particles emitted from the source's edges at an angle  $\delta$  relative to the optimum focus angle  $\gamma$  shown by the dashed lines in the figure. Particles in front of F ( $u \ge f_u$ ) are focused at  $F_f$ , while those behind  $F(u < f_u)$  are focused at  $F_h$ . Although this ad hoc approach provides a practical framework for modelling, it may not accurately reflect the physical trajectories of particles emitted from the source.

Expressions for the geometrical angles  $\phi$ ,  $\xi$ ; focal positions  $f_f$  and  $f_b$ , and beam width (standard deviation)  $\sigma_f$  at a point  $P = (p_u, p_v)$  are:

$$\gamma = \tan^{-1} \frac{\sigma}{f_u} \tag{45}$$

$$\xi = \gamma + \delta \tag{46}$$

$$\phi = |\gamma - \delta| \tag{47}$$

$$f_f = \frac{\sigma}{\tan \xi} \tag{48}$$

$$f_b = \frac{\sigma}{\tan(\gamma - \delta)} \tag{49}$$

$$\sigma_f = \begin{cases} |f_b - p_u| \tan \phi, & p_u < f_u \\ |p_u - f_f| \tan \xi, & p_u > f_u \\ f_u \tan(\gamma + \delta) - \sigma, & p_u = f_u \end{cases}$$

$$(50)$$

In the limit,  $f_u \gg \sigma$  and  $\delta \ll 1$ 

$$\gamma = \frac{\sigma}{f_{u}} \tag{51}$$

$$f_f = \frac{\sigma}{\gamma + \delta} \tag{52}$$

$$f_b = \frac{\sigma}{\gamma - \delta} \tag{53}$$

$$\sigma_f = f_u \delta \qquad (p_u = f_u) \tag{54}$$

The velocity is taken to be normally distributed  $\mathcal{N}(\theta_u^b(p_u, p_v), \delta^2)$  where:

$$\theta_{\mu}^{b}(p_{u}, p_{v}) = \begin{cases} \tan^{-1}\left(\frac{-p_{v}}{f_{b} - p_{u}}\right), & p_{u} < f \\ \tan^{-1}\left(\frac{p_{v}}{p_{u} - f_{f}}\right), & p_{u} \ge f \end{cases}$$
(55)

In the case  $\delta > \gamma$ ,  $f_b < 0$  and the beam model is modified as shown in Fig. 6. In this case the beam divergence dominates the focussing of the beam even in the near-focus region  $u < f_u$ . Equations (45) to (55) remain valid. In the MAST Upgrade case,  $f_u = 12m$ , w/2 = 82.5 mm,  $\delta = 0.6$ degrees yielding  $\gamma = 0.39$  degrees. Therefore we are in the regime  $\delta > \gamma$ and the results presented use the model shown in Fig. 6.

In both the Bannmann model and the analytic model presented in Section 2, the velocity is normally distributed, though in the latter case it has truncated bounds. In the Bannmann model, the mean velocity depends on one of two virtual focal positions (see equations (55)) and the standard deviation is constant. In contrast, the analytic model has a single focal point and a position-dependent standard deviation of velocity (cf.  $\sigma_{\star}(p_u)$  in equation (30)).

## 3.1. Results

Fig. 7 plots the spatial variation at six discrete values of  $p_u$ . From inspection of the figure:

- 1. The agreement between the analytic model and the ray-tracing model is excellent for all values of  $p_u$ . The distribution is not a normal apart from at the positions  $p_u$  and  $p_u = f$ .
- 2. At  $p_u = 0$  (the source location) the distribution for all three cases is a truncated normal distribution in agreement with the requirements of the model.

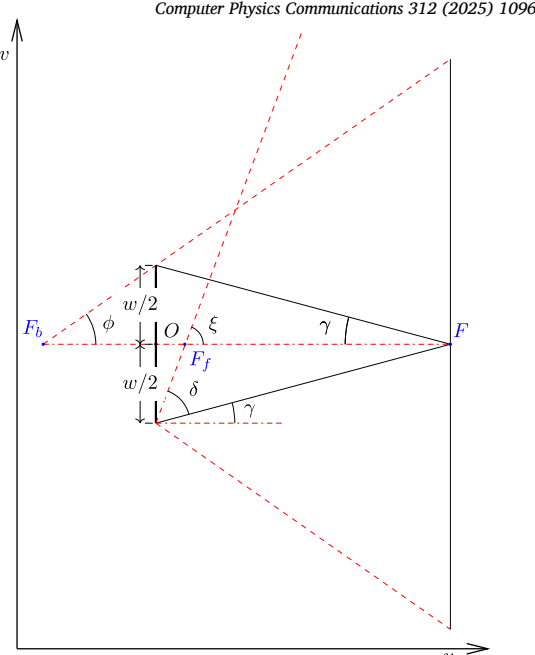


**Fig. 6.** Geometrical depiction of a single Gausscil beam  $(\delta > \gamma)$  [18].

- 3. At  $p_u = 12m$  (the "focal-plane") the Bannmann model is in agreement with the analytic model and ray tracing model. This is the case because  $f_u \gg \sigma$  and  $\delta \ll 1$  and equation (54) applies i.e.  $\sigma \approx f_u \delta$ , the value for the analytic model (see section 2.1, observation 3(b)).
- The Bannmann model does not agree perfectly with the analytic model and ray-tracing results away from  $p_u = 0$  and  $p_u = f$ .

Fig. 8 plots the velocity distribution at  $p_v = 0$ ,  $p_v = \sigma_r$  and  $p_v = 2\sigma_r$ at three positions along the beam:  $p_u = 0$ ,  $p_u = 12m$ , and  $p_u = 20m$ . There is no plot at  $p_u = 0$ ,  $p_v = 2\sigma$  as the beam is truncated spatially at  $p_v = \sigma$ . From inspection of the figure and the model equations:

- 1. The agreement between the analytic model and the ray-tracing model is excellent for all cases. This includes the details of the truncation limits.
- 2. The Bannmann model agrees with the ray-tracing model and analytic model only at the mid-point of the source (see the left-hand graph in Fig. 8(a)). The use of a virtual focus position  $(F_h)$  rather than the true focal position (F) explains the discrepancy in the right plot of Fig. 8(a). The assumption that the velocity standard deviation is  $\delta$ , independent of position, yields values that are at too large at  $p_u = 12m$  and  $p_u = 20m$ . Finally the Bannmann model assumes the distributions are unbounded in comparison with the analytic model that provides truncation bounds for  $p_u > 0$ .

In conclusion, agreement between the analytic model and ray-tracing model is excellent in all cases. The reason that the Bannmann model works well for interpretation of Charge Exchange Recombination Spectroscopy (CXRS) data [19] is explained by the fact that the details of the velocity distribution are not important in this case.

## 4. Transmission losses

Transmission losses in neutral beamlines occur when obstructions, such as baffles, intercept portions of the beam, effectively "scraping" off its edges. For a point P downstream of an obstruction at coordinates  $B = (b_u, b_v)$  (refer to Fig. 2), the obstruction angle  $\theta_b$  is defined as:

$$\theta_b = \tan^{-1}\left(\frac{p_v - b_v}{p_v - b_v}\right) \tag{56}$$

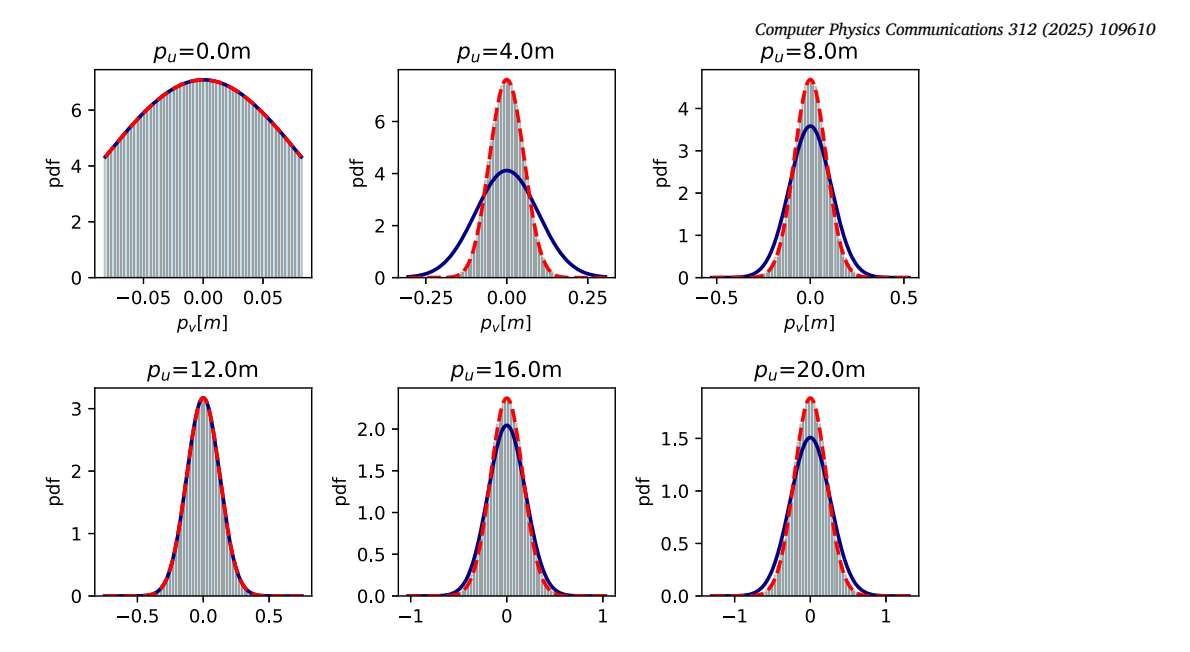


Fig. 7. Comparison of  $g_2(p_v; p_u)$  (red line) with ray tracing calculation (histogram) and the Bannmann [18] model (blue line). The results are shown for six  $p_u$  values;  $p_u = 0$  is the source location,  $p_u = 12m$  is the focal plane.

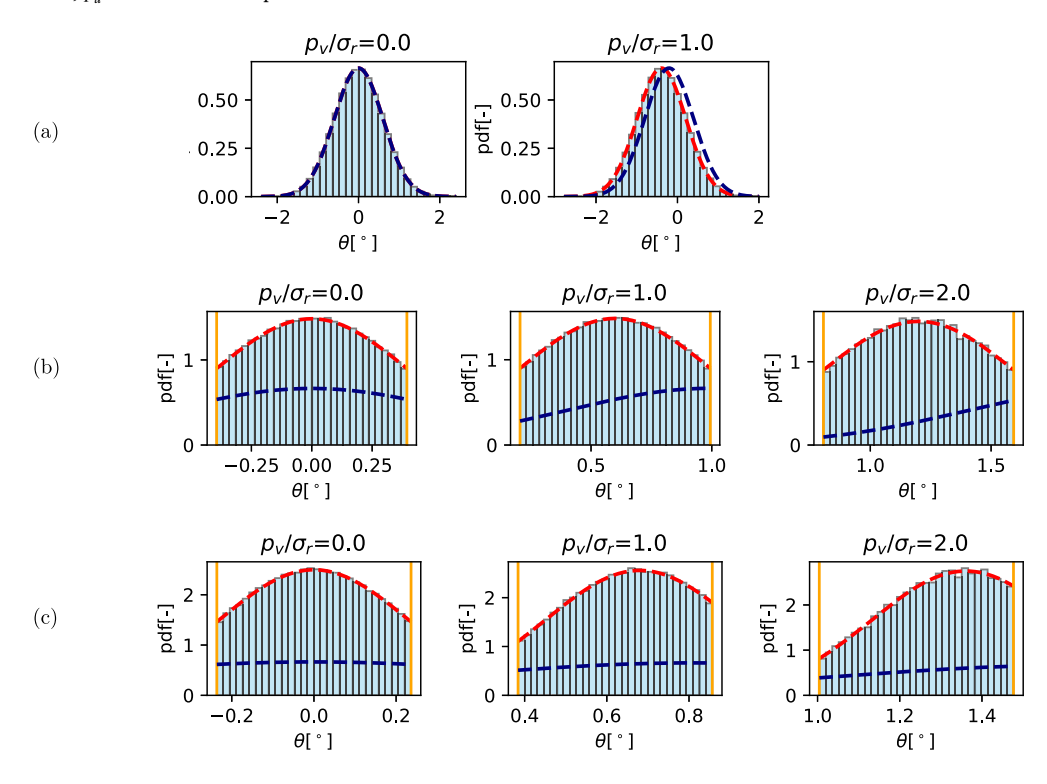


Fig. 8. Comparison of  $g_1(\theta, p_u; p_u)$  (red dashed line with the truncation limits shown in orange); ray tracing calculation (histogram); and Bannmann [18] model (blue dashed line). Results are shown for: (a)  $p_u = 0$ , the source location; (b)  $p_u = 12m$ , (plane through focal point); (c)  $p_u = 20m$ .

Obstructions intercepting the top of the beam are denoted as  $\theta^t_b$  and those intercepting the bottom as  $\theta^b_b$ . The sets of these obstructions downstream of point P are  $\theta^t_b = \{\theta^t_{b_1}, \dots, \theta^t_{n_t}\}$  and  $\theta^b_b = \{\theta^b_{b_1}, \dots, \theta^b_{n_b}\}$ , respectively. Equations (33) and (34) impose constraints on the permissible angles:

$$\theta_{\min} < \theta < \theta_{\max} \tag{57}$$

The presence of obstructions introduces an additional constraint:

$$\max(\boldsymbol{\theta}_{b}^{t}) < \theta < \min(\boldsymbol{\theta}_{b}^{b}) \tag{58}$$

Combining these inequalities results in:

$$\max(\theta_b^t, \theta_{\min}) < \theta < \min(\theta_b^b, \theta_{\max})$$
 (59)

This combined constraint ensures that only beam trajectories unobstructed by baffles contribute to the transmission at point P. Taking account of transmission losses simply requires to update the values of  $\theta_{\min}$  and  $\theta_{\max}$  in equations (33) and (34) with these new limits (i.e.  $\theta_{\min} \to \max(\theta_b^l, \theta_{\min})$  and  $\theta_{\max} \to \min(\theta_b^b, \theta_{\max})$ ). Equations (39) and (40) are transformed in a similar manner.

Reducing the permissible pitch angles affects both the velocity and radial distribution functions,  $g_1(\theta; p_u, p_v)$  and  $g_2(p_v; p_u)$ , respectively,

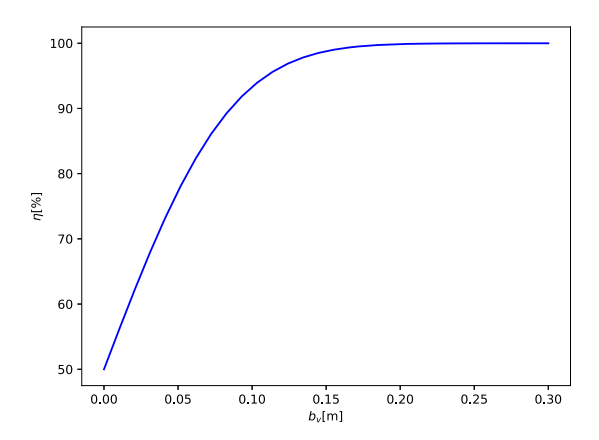


**Fig. 9.** Transmission efficiency for MAST Upgrade case with an obstruction at u = 6m, descending into the beam in the range  $0 < b_v < 0.3m$ . The result shown is for  $p_u > 6m$ .

through the term  $n_2$  (equation (35)). The modified PDF  $g_1(\theta; p_u, p_v)$  retains the property  $\int g_1(\theta; p_u, p_v) d\theta = 1$ . However the integral of  $g_2(p_v; p_u)$ :

$$\eta = \int g_2(p_v; p_u) dp_v \tag{60}$$

represents the transmission efficiency; a value of  $\eta < 1$  indicates that some particles have been intercepted by obstructions before reaching  $u = p_u$ . Evaluating  $\eta$  typically involves numerical integration. Since the integral is one-dimensional over a smooth function, it is readily evaluated using Gaussian quadrature.

Fig. 9 illustrates the variation in  $\eta$  for a single obstruction located at u=6 m, where the beam is intercepted from above  $(v>b_v)$ . The figure shows that for values of  $p_u$  downstream of the obstruction,  $\eta$  varies between 50% and 100%, depending on the value of  $b_v$ . Upstream of the obstruction,  $\eta$  remains constant at 100%.

# 5. Non-Gaussian 1-D source distributions

In this section, we generalize the spatially truncated normal distribution assumption at the source to accommodate "arbitrary" distributions. This is accomplished by representing the source distribution as a set of spatially distributed truncated Gaussian basis functions.

The PDF,  $\Gamma(q,\theta)$ , constructed from a collection of  $n_b$  normally distributed sources with truncated bounds, is expressed as:

$$\Gamma(q,\theta) = \sum_{k=1}^{n_b} \Gamma_k g_k(q,\theta)$$
 (61)

where  $g_k(q, \theta)$  represents the PDF of a single Gaussian source with spatial truncation (cf. equation (4)):

$$g_k(q,\theta) = \begin{cases} \frac{A_k}{n_{2_k}} \exp\left(-\frac{(q-q_k)^2}{2\sigma_k^2} - \frac{(\theta-\theta_\mu)^2}{2\delta^2}\right) \\ \text{if } q_{min} \le q \le q_{max} \text{ and } -\frac{\pi}{2} \le \theta \le \frac{\pi}{2} \\ 0 \text{ otherwise} \end{cases}$$
 (62)

Here the normalisation constant  $A_k$  and the terms  $n_{1_k}$ ,  $n_{2_k}$ , are defined as:

$$A_k = \frac{1}{2\pi\sigma_k \delta n_1} \tag{63}$$

$$n_{1_k} = \Phi\left(\frac{q_{max}}{\sigma_k}\right) - \Phi\left(\frac{q_{min}}{\sigma_k}\right) \tag{64}$$

$$n_{2_k} = \Phi\left(\frac{\pi/2 - \theta_{\mu_k}}{\delta}\right) - \Phi\left(\frac{-\pi/2 - \theta_{\mu_k}}{\delta}\right)$$
 (65)

For each  $g_k(q,\theta)$ , the expressions for the PDFs  $g_1(\theta;p_u,p_v)$  and  $g_2(p_v;p_u)$  are given by equations (22) to (44) with the transformation  $p_v\to p_v-q_k$ .

For  $\Gamma(q,\theta)$  to be a probability requires that  $\sum_{k=1}^{n_b} \Gamma_k = 1$ . With this condition satisfied,  $\Gamma_k$  is the fractional flux carried by the  $k^{th}$  basis function

To set about defining parameters of the constituent basis functions to fit a given distribution, we integrate equation (61) over  $\theta$ :

$$\Gamma^{r}(q) = \sum_{k=1}^{n_b} \Gamma_k g_k^r(q) \tag{66}$$

where the marginal distribution  $g_{L}^{r}(q)$  is:

$$g_k^r(q) = \begin{cases} \sqrt{2\pi} A_k \delta \exp\left(-\frac{(q - q_k)^2}{2\sigma_k^2}\right) & q_{min} \le q \le q_{max} \\ 0 & \text{otherwise} \end{cases}$$
 (67)

With defined  $q_k$  and  $\sigma_k$  values, the set of coefficients  $\Gamma_b = \{\Gamma_1, \cdots, \Gamma_{n_b}\}$  can be determined in a least-squares sense by solving a set of linear equation, with the stiffness matrix composed of  $g_k^r(q_i)$  terms evaluated at a set of  $n_s$  sample points  $q_i \in \{q_1, \cdots, q_{n_s}\}$  distributed over the one-dimensional source domain:

$$\begin{bmatrix} g_1^r(q_1) & \cdots & g_{n_b}^r(q_1) \\ \vdots & \ddots & \vdots \\ g_1^r(q_{n_s}) & \cdots & g_{n_b}^r(q_{n_s}) \end{bmatrix} \begin{bmatrix} \Gamma_1 \\ \vdots \\ \Gamma_{n_b} \end{bmatrix} = \begin{bmatrix} \Gamma^r(q_1) \\ \vdots \\ \Gamma^r(q_{n_s}) \end{bmatrix}$$
(68)

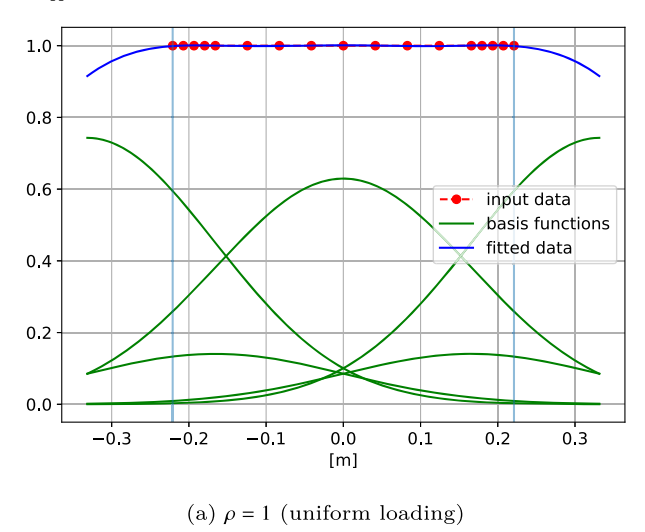
Selecting appropriate values for  $q_k$  and  $\sigma_k$  is crucial for achieving a smooth fit across the data range, minimizing artefacts such as ringing, especially at the boundaries, and ensuring that all basis function amplitudes are positive (i.e.  $\Gamma_i > 0, \forall i \in \{1,2,\ldots,n_b\}$ ). In addition as discussed in section 7 the choice of basis function affects the calculation accuracy of the transmission efficiency.

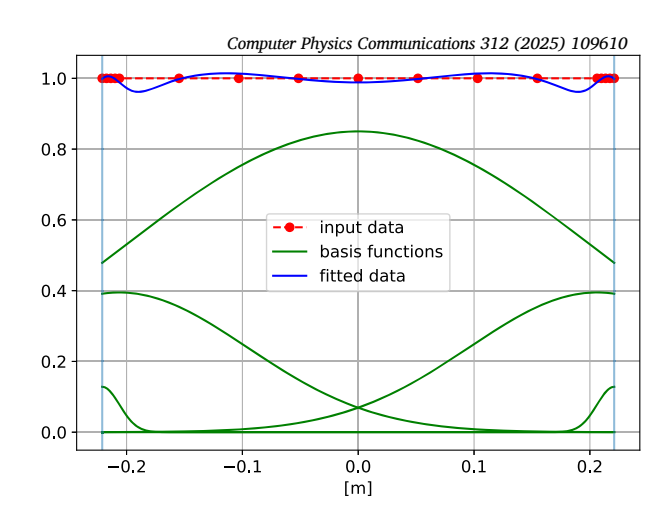
A single parameter,  $\rho$ , controls the 1-D spatial density of the basis functions via a power-law distribution,  $q^{\rho}$ . Here,  $\rho=1$  corresponds to a uniform distribution,  $\rho>1$  increases density toward the beam center, and  $\rho<1$  increases density toward the periphery. To mitigate ringing effects, the number of constraint points is increased proportionally to the basis function density. The standard deviation of each basis function is set equal to the distance to its nearest neighbour (or the average distance, in cases of non-uniform distribution) further enhances the fit

Numerical tests demonstrate that for  $\rho>0.1$  excellent fits are obtained to a set of constant values,  $\Gamma^r(q_i)=1$  with  $q_{min}\leq q_i\leq q_{max}$  by placing the mean positions of basis functions within a spatial range extending one standard deviation beyond the physical extent of the beam source. A particular example with  $\rho=1$  is shown in Fig. 10(a). All observed computed fits have no ringing and with basis function amplitudes that are always positive. Obtaining good fits with  $\rho=0.1$  is more challenging, because of the reduced density of basis functions in the domain interior. Fig. 10(b) shows a typical case for  $\rho=0.1$  and was obtained with the mean positions of basis functions restricted to lie within the range of the source domain. Compared to the previous case, ringing is apparent in the domain interior. Other tests have negative amplitudes for basis functions with means close to the domain boundaries. This is strictly permissible numerically and is not inconsistent physically as the sum of the basis functions is nevertheless greater than zero at all values of q.

#### 6. Extension to 2-D source distributions

The model can be extended to two dimensions if the beam can be approximated as rectangular and is uncorrelated across dimensions. For cases involving multiple beams (e.g., beamlets within a larger beam), the constraints apply individually to each beamlet rather than to the composite beam. The PDF at the source grid can then be expressed as the product of two independent distributions:





(b)  $\rho = 0.5$  (high density of basis functions at boundaries).

Fig. 10. Results of fitting a set of data with 5 basis functions. The blue curve represents the sum of the constituent basis functions, which are individually shown in green. The boundary of the region, indicated by faint blue vertical lines, is located at  $\pm 0.21$  m.

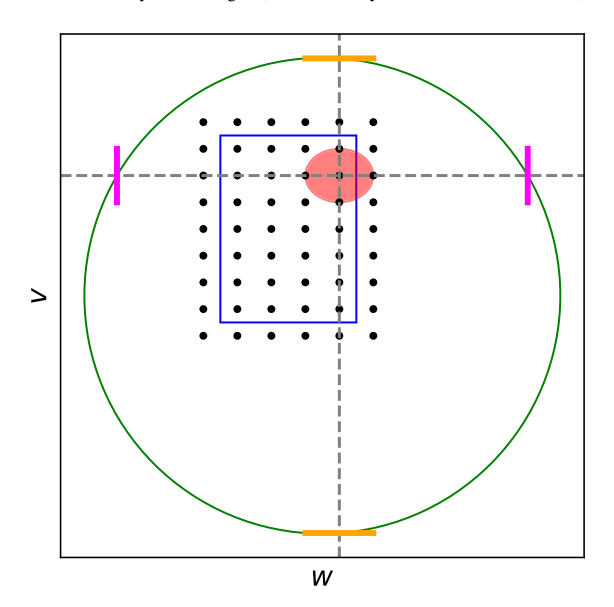


**Fig. 11.** Cartoon of a 2-D beam source, indicating the locations of Gaussian basis functions. The shaded region indicates the range to within one standard deviation for a single Gaussian basis function. The green circle indicates the position of a circular baffle surface, and the magenta and orange lines indicate the positions of effective baffles necessary to compute the 1-D beam propagation in the v-u and w-u planes respectively.

$$g(q_{uv}, \theta_{uv}, q_{wu}, \theta_{wu}) = g_{uv}(q_{uv}, \theta_{uv})g_{wu}(q_{wu}, \theta_{wu})$$
(69)

Here  $g_{uv}$  and  $g_{wu}$  corresponds to  $g(q,\theta)$  as defined in equation (4). The function  $g(q_{wu},\theta_{wu})$  is obtained by transforming  $g(q,\theta)$  with the substitutions  $w\to -v$  and  $\theta_{wu}\to -\theta$ .

An additional condition is that the baffle edges must align with the beam-aligned uww coordinate system. However, this is not achievable for circular baffles and may only be partially true for other baffles shapes. Accurate modelling of baffle losses necessitates precise boundary representation, considering combinations of rectangular and circular baffles, as illustrated in Fig. A.19.

To address this challenge, the source distribution can be decomposed into Gaussian basis functions each occupying a smaller spatial extent, as outlined in Section 5. Fig. 11 shows the arrangement of Gaussian basis functions over a two-dimensional source grid, uniformly distributed on a grid, aligned with the coordinate axes. Defining the source intensity distribution as the product of two one-dimensional functions:

$$\Gamma^{r}(v,w) = \Gamma^{r}_{v}(v)\Gamma^{r}_{w}(w) \tag{70}$$

permits the node intensities to be computed in one dimension by solving equations (68) separately for each axis using  $\Gamma^r(q_i)$  sets generated from the functions  $\Gamma^r_v(v)$  and  $\Gamma^r_w(w)$ . From these results, the two-dimensional PDF can be assembled.

The independence of the distributions in the uv, and vw planes allows the transmission coefficient,  $\eta$ , to be computed as a sum of products of integrals over  $n_b$  basis functions:

$$\eta = \sum_{k=1}^{n_b} \Gamma_k \int \left( g_{uv} \right)_2^k dv \int \left( g_{wu} \right)_2^k dw \tag{71}$$

Here,  $(g_{uv})_2^k$  denotes the  $k^{th}$  basis function's  $g_2$  PDF (equation (28)) in the uv plane, and  $(g_{wu})_2^k$  represents the  $k^{th}$  basis function's  $g_2$  PDF in the wu plane.

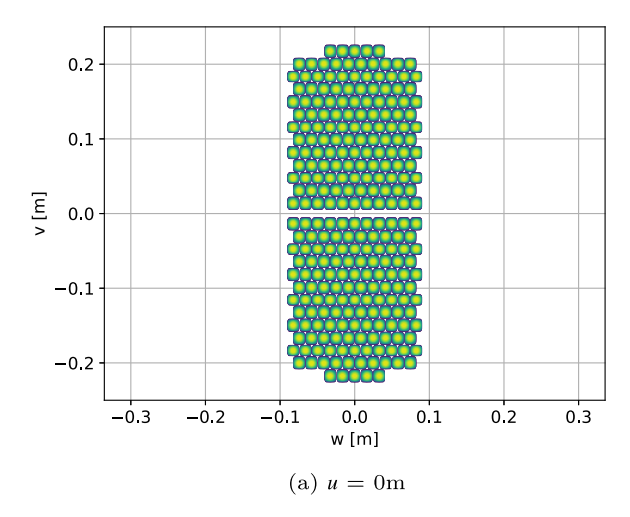
The next section will explore how the selection of the number of basis function and their spatial distribution influences the model's capacity to accurately account for baffle-induced losses.

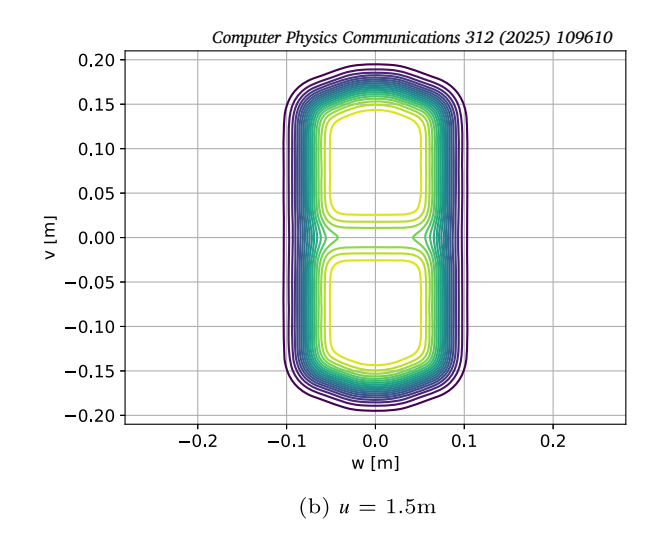
# 7. Application to MAST Upgrade

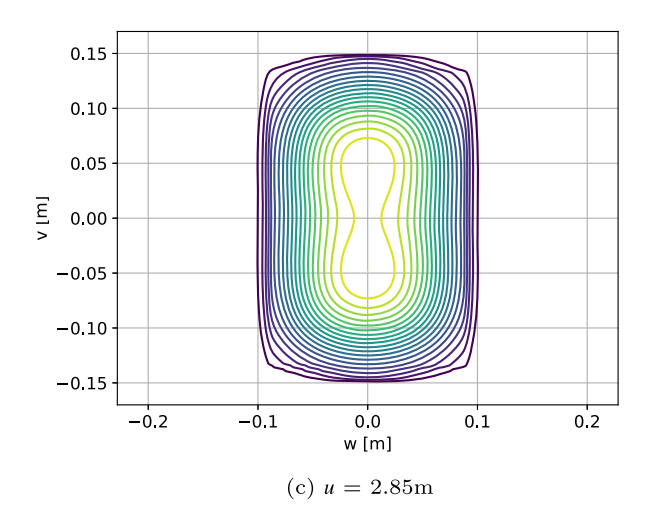
A new module has been developed within Minerva to model collisionless beam propagation from a two-dimensional beam source comprising multiple sub-beamlets, incorporating realistic baffle geometries. This enhancement leverages Minerva's recent integration with the ITER Integrated Modelling & Analysis Suite (IMAS) [33,34], enabling the simulation of any neutral beam system for which an appropriate IMAS database instance is available. In this section, we present model predictions for the MAST Upgrade neutral beam system.

The MAST neutral beam system is detailed in Barrett [35], with additional engineering specifications provided in a technical note [31]. As the latter information is not publicly available, we include pertinent details here, along with descriptions of baffles and PINI geometry in the appendix.

The IMAS dataset for the MAST Upgrade beam system specifies the locations of 262 beamlets and their fractional powers; in the data set used for this work there is equal power distribution among all beamlets. The numerical model computes the PDF of the beam by summing the contributions from each beamlet. To reduce computational demands, the model also allows for fitting the spatial variation of fractional powers with a reduced set of basis functions, as described in Section 5. Below, we present results using both the full set of 262 beamlets (*method 0*) and the reduced set of basis functions (*method 1*).







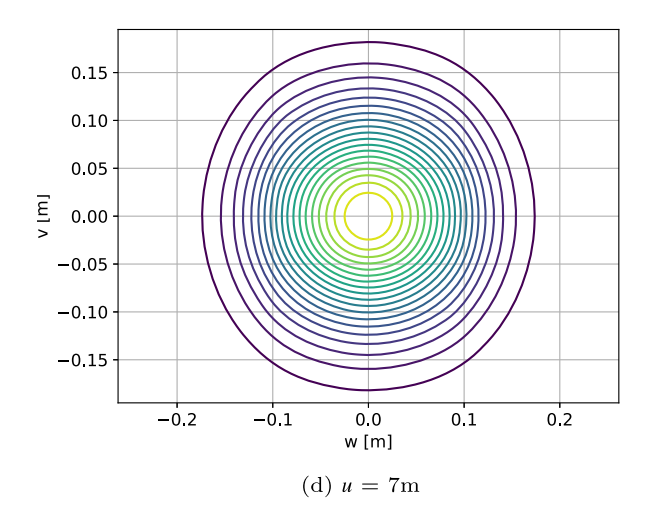
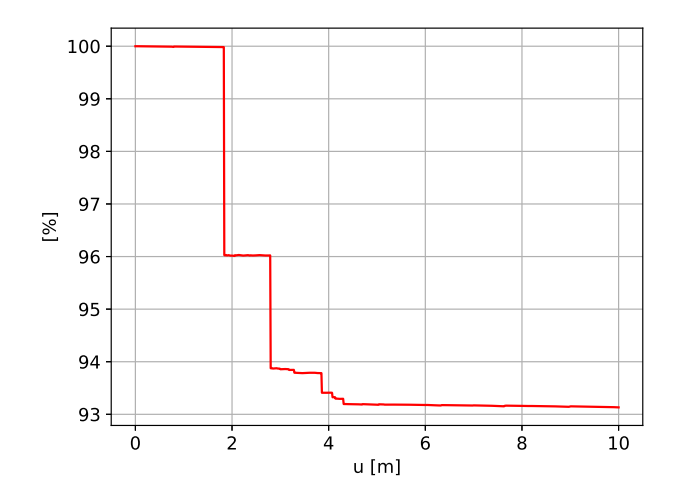


Fig. 12. Variation of PDF on planes normal to the MAST Upgrade neutral beam source marginalised over velocity.

Fig. 12 displays contours of PDF variation, marginalized over velocity, for a MAST Upgrade neutral beam using *method 0*. The plots are on planes parallel to the beam source, with u denoting the normal distance from the source. Figures are shown at the beam source (u = 0 m), at two positions downstream toward the plasma cavity (u = 1.5 m and u = 2.5 m), and within the plasma cavity (u = 7 m). The coordinates v and w represent vertical and horizontal positions relative to the center of the beam source.

In Fig. 12(a), the localized intensity of the 262 beamlets is evident, exhibiting symmetrical mirroring across the beam source. The PDF in subsequent panels (Figs. 12(b–d)) is modified by the combined effects of velocity divergence and baffle interactions. Notably, the shaping observed in Fig. 12(b) results from the "Neutraliser II HR" baffle, the outline in Fig. 12(c) is due to the "Inter-tank duct entry" baffle, and the circular outline in Fig. 12(d) arises from the "Duct 1 entry" baffle (see Table A.4 for baffle names and coordinates).

Fig. 13 illustrates the variation in transmission efficiency with distance from the beam source, calculated using *method 0*. Step-wise reductions in efficiency are induced by baffles, resulting in a final transmission efficiency of  $\eta=93.2\%$  at the plasma cavity. The most significant degradations occur at the "Neutraliser II HR" baffle (u=1.840 m), the "Inter-tank duct entry" baffle (u=2.799 m), and the "Duct 1 entry" baffle (u=3.851 m). These results align with calculations of transmitted power efficiency in the JET beam line, as shown in figure 8 of [26]. Although [26] does not provide specific details about the beam geometry,



**Fig. 13.** Variation of transmission efficiency for a MAST Upgrade neutral beam as a function of distance from the beam source.

beam divergence and baffle geometry, the reported transmission efficiency of  $\eta=88\%$  for JET, obtained using the PINI simulator code, is reassuringly close to the value computed for MAST Upgrade.

Fig. 14 compares transmission efficiency at u = 7 m across five model variants. The dashed line represents results from *method 0*, considered

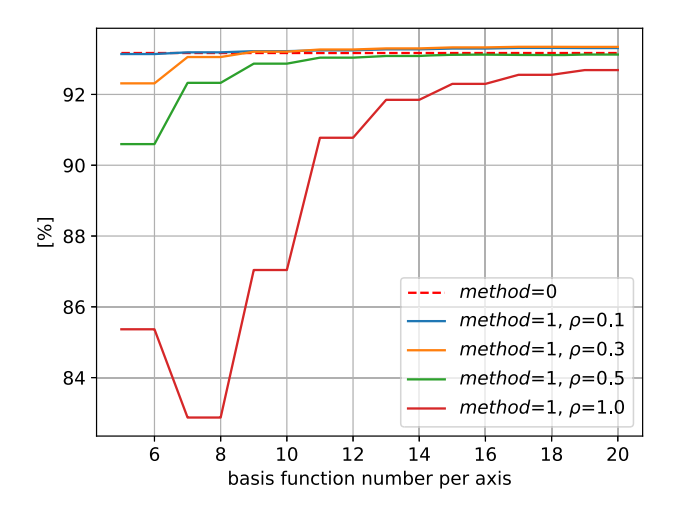
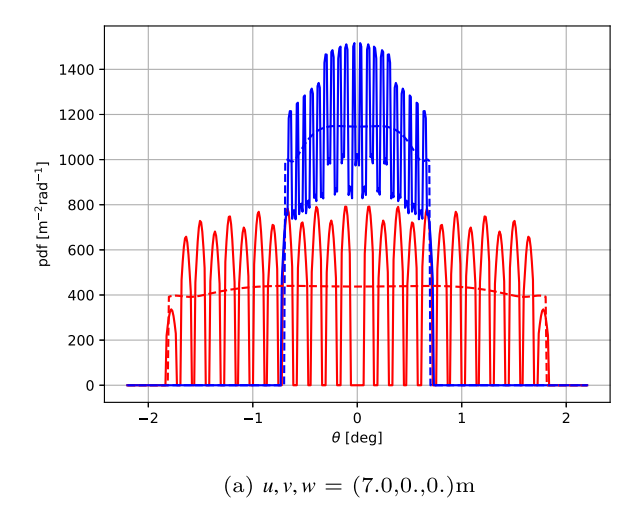
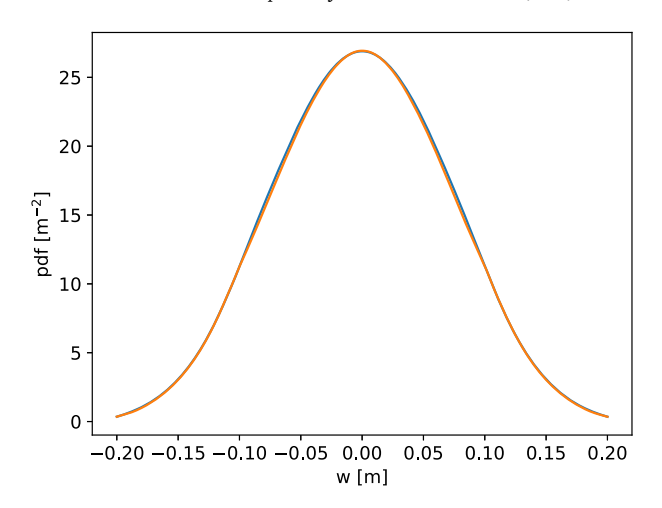


Fig. 14. Comparison calculations of transmission efficiency at u = 7 m.





**Fig. 15.** Horizontal profile of power density, marginalised over velocity at u = 7 m and v = 0 m.

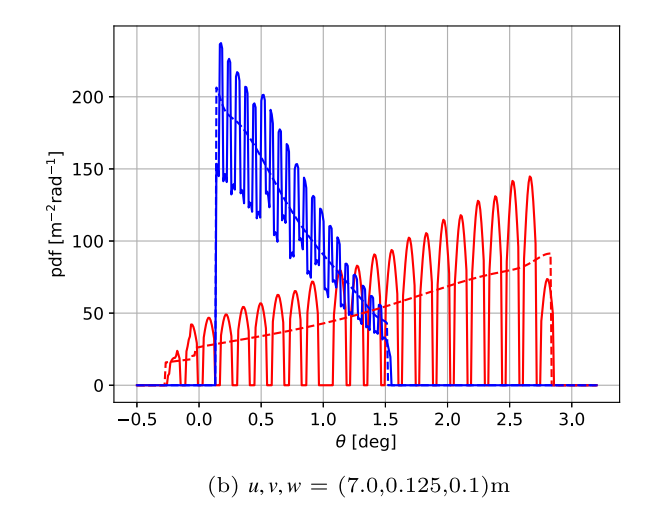


Fig. 16. Marginal velocity distributions in the wu plane (blue) and in the vu plane (red). The angle  $\theta$  is the anti-clockwise angle subtended by the velocity vector with the unit vector in the u-direction. Results shown are from model  $method\ 0$  (solid line) and  $method\ 1$  (dashed line). Refer to Fig. 12d to relate the velocity distributions to their spatial positions within the neutral beam.

the most accurate representation of the neutral beam system. Other calculations employ alternative sets of basis functions as prescribed in Section 5. The findings show that as the density of basis functions changes from uniform loading to edge loading ( $\rho = 1.0 \rightarrow \rho = 0.5 \rightarrow \rho = 0.3 \rightarrow$  $\rho = 0.1$ ), the discrepency with the *method 0* result decreases. In particular the result with  $\rho = 0.1$  and 5 basis functions per axis is within 0.03% of the method 0 result. Further calculations show that for these model parameters the maximum discrepency in the transmission efficiency in the range 0 < u < 10 is 0.25%. The reason that small values of  $\rho$  improve accuracy is because the generated basis functions can better account for circular baffles; in cases where the baffles are entirely parallel to the v- or w- axes there was no observed dependence on  $\rho$ . These results show that using five basis functions per axis (totalling 25 basis functions) results in a transmission efficiency degradation of less than 0.03% at u = 7 m (0.25% for u < 10 m), while reducing execution time by a factor of approximately 10. It is important to note that method 0 and method 1 address similar but not identical problems. While method 0 models a non-rectangular, locally varying source distribution,  $method\ 1$  assumes a rectangular source with a constant (and, in this work, non-varying) fractional power density. For method 1 the transmission efficiency is affected by the dimensions of the nominal source; the results shown in Fig. 14 assumed the dimensions of the rectangular beam source extended 3 mm (i.e. one PINI half-radius) beyond the outer PINI beamlets.

Fig. 15 presents the horizontal PDF profile, marginalized over velocity, at u=7 m and v=0 m. Results are shown for *method 0* and *method 1* ( $\rho=0.1$  with five basis functions per axis). The two cases are nearly indistinguishable, indicating that the simplified model accurately represents spatial variations in the neutral beam at this location.

Fig. 16 plots the marginal velocity distributions in the wu and uv planes at u=7 m. Results for  $method\ 0$  and  $method\ 1$  (using  $\rho=0.5$  with five basis functions per axis) are compared. The  $method\ 0$  results exhibit detailed variations reflecting the spatial distribution of beamlets on the source grid. In particular, the unusual  $\theta$ -dependence in the wu plane is due to fewer beamlets on the top and bottom rows of the beamlet grid (see Fig. 12a). In all cases the  $method\ 1$  results closely replicate the trends of the  $method\ 0$  results. These plots show that the effect of superposing the spatially offset Gaussian beams results in velocity distributions that are fundamentally different to the distribution of a single Gaussian beam expressed by equation (27) (cf. Fig. 8).

#### 8. Conclusions

We have developed an analytical model to describe the transport of collisionless particles in neutral beam systems, incorporating non-Gaussian source distributions using Gaussian basis functions. The model extends to two-dimensional source distributions under the assumption of separability along orthogonal axes, enabling a comprehensive analysis of beam propagation dynamics.

The model also accounts for baffle geometry, with reductions in the transmission factor due to baffle losses computed efficiently through integrals over one-dimensional marginal velocity distributions along each beam axis. The model shows that a single beam's velocity distribution retains its Gaussian nature en route to the plasma cavity, although its divergence is modified by geometric shaping. However, superposing spatially offset Gaussian beams can produce a velocity distribution that deviates significantly from a Gaussian profile (see Fig. 16). The degree of deviation will depend on the spatial distribution of fractional beam power among the Gaussian components.

Our implementation of the model as a module in Minerva, interfaced with IMAS, enables the computation of two-dimensional collisionless particle distributions for any neutral beam system with an available IMAS database. Application to the MAST Upgrade neutral beam system has demonstrated the model's ability to account for detailed source distributions and to capture the evolving beam shape and velocity distribution.

A key feature of the model is its computational efficiency. By employing an analytical method to evolve the particle distribution instead of relying on Monte Carlo tracking of individual particles, the model ensures computational tractability, particularly in Bayesian analysis contexts. Using a reduced basis set to represent the source distribution maintains accuracy within 0.25% for transmission efficiency calculations, while achieving a tenfold reduction in execution time.

Future plans involve coupling the collisionless beam model with a collisional-radiative model to enhance diagnostic modelling capabilities, enabling the quantification of beam losses in the duct during its transit to the plasma cavity. Additionally, the implementation of the model within the Minerva framework, achieved during the current work, will create new opportunities to address uncertainty-related challenges in neutral beam systems within the tokamak context by utilizing the extensive Bayesian analysis tools provided by Minerva.

This integration will particularly benefit diagnostics such as Motional Stark Effect (MSE) and Charge Exchange Recombination Spec-

troscopy (CXRS) on MAST Upgrade. By applying Bayesian analysis, uncertainties in parameters such as beam divergence, power flux, geometry, and the neutral gas distribution in the duct can be systematically evaluated. This comprehensive approach will enhance the interpretation of diagnostic data and optimize the performance of heating systems in tokamaks reliant on neutral beams.

#### **Declaration of competing interest**

The authors declare that they have no known competing financial interests or personal relationships that could have appeared to influence the work reported in this paper.

#### Acknowledgements

The Author would like to thank the useful discussions that he has had with the UKAEA neutral beam group, especially to Dave Keeling, Damian King, Ian Day, Roy McAdams and Maria Nicosia. In addition he would like to thank Sam Blackmore in the UKAEA diagnostics group, Sebastian Bannmann at IPP Greifswald and Clive Michael at the Physics and Astronomy Department, UCLA for their generous support and advice in formative discussions. Finally he would like to express sincere gratitude to Udo Hoefel and Jakob Svensson for support in the use of Minerva.

This work has been funded by the EPSRC Energy Programme [grant number EP/W006839/1]. To obtain further information on the data and models underlying this paper please contact PublicationsManager@ukaea.uk.

For the purpose of open access, the author(s) has applied a Creative Commons Attribution (CC BY) licence (where permitted by UKRI, 'Open Government Licence' or 'Creative Commons Attribution No-derivatives (CC BY-ND) licence' may be stated instead) to any Author Accepted Manuscript version arising.

# Appendix A. The MAST neutral beam system

Fig. A.17 shows the engineering dimensions of the MAST neutral beam system. The values of parameters referred to in this figure are given in Table A.1. Other relevant design parameters are given in Table A.2. The final acceleration grid (referred to as *grid 4* in Fig. A.17) is shown in Fig. A.18. Ions emerge from 262 circular holes each with a diameter of 12 mm into a neutralisation chamber. The coordinates of the sub-beamlets are provided in Table A.3 and baffle coordinates in Table A.4. The locations of the beam baffles are plotted in Fig. A.19.

**Table A.1**Neutral beam engineering dimensions (see Fig. A.17 for parameters definitions). Taken from [31].

Engineering Dimension	Parameter Values / mm (unless stated)			
88	sector 6	sector 8		
Beamline ID	SS	SW		
R, Tangency radius	705.7	800		
$R_p$ Pivot radius	2063.3	2103.5		
$Z_s^r$ beamline length	5112.9	5068.3		
Y <sub>s</sub> Vertical offset	0	650		
$\alpha_s$ inclination angle	0°	0°		

**Table A.2**Neutral beam design parameters operated with Deuterium injection. Taken from [31].

Description	Parameter Values
Maximum beam energy	75kV
Maximum beam current	65A
Beamlet divergence angle (at maximum current and voltage)	0.6°
Grid half-height	218 mm
Grid half-width	82.5 mm
Horizontal focal length	14 m
Vertical focal length	6 m

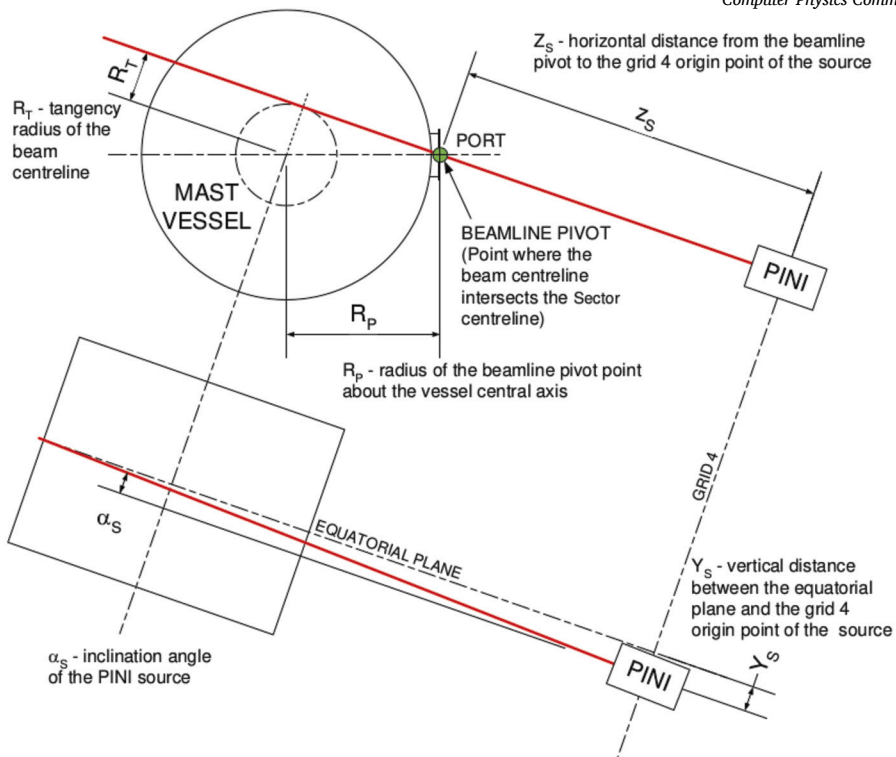


Fig. A.17. "Engineering" dimensions of the MAST neutral beam system (taken from [31]).

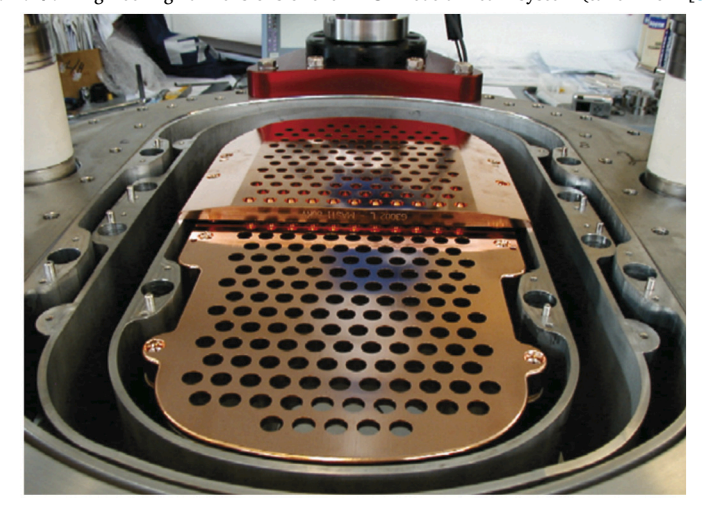


Fig. A.18. "The final-stage acceleration grid (referred to as grid 4 in Fig. A.17). The grid consists of a lower and upper part.

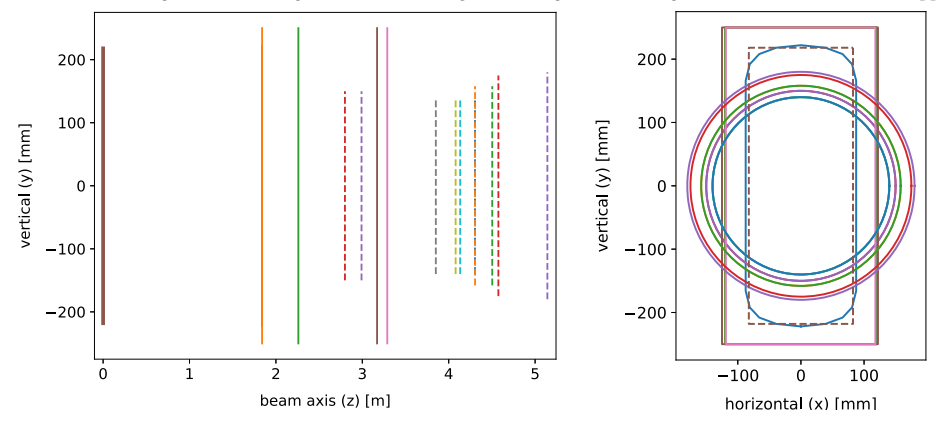


Fig. A.19. Locations of the MAST Upgrade baffles. (left) vertical extent of each baffles. Source grid is indicated as a thick line at z = 0m and circular baffles are shown as dashed lines; (right) vertical and horizontal extent of baffle. The source grid is shown as a dashed line.

 $\textbf{Table A.3} \\ \textbf{Centroid locations of the 262 sub-beamlets in w,v (width and height) coordinates on the final acceleration grid. Coordinate are shown with respect to the centre of the grid.}$ 

w	υ	w	υ	w	υ	w	υ	w	υ	w	υ
-0.0825	0.0135	-0.0825	0.1495	0.04125	0.0645	-0.066	-0.0135	-0.066	-0.1495	0.05775	-0.0645
-0.066	0.0135	-0.066	0.1495	0.05775	0.0645	-0.0495	-0.0135	-0.0495	-0.1495	0.07425	-0.0645
-0.0495	0.0135	-0.0495	0.1495	0.07425	0.0645	-0.033	-0.0135	-0.033	-0.1495	-0.07425	-0.0985
-0.033	0.0135	-0.033	0.1495	-0.07425	0.0985	-0.0165	-0.0135	-0.0165	-0.1495	-0.05775	-0.0985
-0.0165	0.0135	-0.0165	0.1495	-0.05775	0.0985	0.	-0.0135	0.	-0.1495	-0.04125	-0.0985
0.	0.0135	0.	0.1495	-0.04125	0.0985	0.0165	-0.0135	0.0165	-0.1495	-0.02475	-0.0985
0.0165	0.0135	0.0165	0.1495	-0.02475	0.0985	0.033	-0.0135	0.033	-0.1495	-0.00825	-0.0985
0.033	0.0135	0.033	0.1495	-0.00825	0.0985	0.0495	-0.0135	0.0495	-0.1495	0.00825	-0.0985
0.0495	0.0135	0.0495	0.1495	0.00825	0.0985	0.066	-0.0135	0.066	-0.1495	0.02475	-0.0985
0.066	0.0135	0.066	0.1495	0.02475	0.0985	0.0825	-0.0135	0.0825	-0.1495	0.04125	-0.0985
0.0825	0.0135	0.0825	0.1495	0.04125	0.0985	-0.0825	-0.0475	-0.0825	-0.1835	0.05775	-0.0985
-0.0825	0.0475	-0.0825	0.1835	0.05775	0.0985	-0.066	-0.0475	-0.066	-0.1835	0.07425	-0.0985
-0.066	0.0475	-0.066	0.1835	0.07425	0.0985	-0.0495	-0.0475	-0.0495	-0.1835	-0.07425	-0.1325
-0.0495	0.0475	-0.0495	0.1835	-0.07425	0.1325	-0.033	-0.0475	-0.033	-0.1835	-0.05775	-0.1325
-0.033	0.0475	-0.033	0.1835	-0.05775	0.1325	-0.0165	-0.0475	-0.0165	-0.1835	-0.04125	-0.1325
-0.0165	0.0475	-0.0165	0.1835	-0.04125	0.1325	0.	-0.0475	0.	-0.1835	-0.02475	-0.1325
0.	0.0475	0.	0.1835	-0.02475	0.1325	0.0165	-0.0475	0.0165	-0.1835	-0.00825	-0.1325
0.0165	0.0475	0.0165	0.1835	-0.00825	0.1325	0.033	-0.0475	0.033	-0.1835	0.00825	-0.1325
0.033	0.0475	0.033	0.1835	0.00825	0.1325	0.0495	-0.0475	0.0495	-0.1835	0.02475	-0.1325
0.0495	0.0475	0.0495	0.1835	0.02475	0.1325	0.066	-0.0475	0.066	-0.1835	0.04125	-0.1325
0.066	0.0475	0.066	0.1835	0.04125	0.1325	0.0825	-0.0475	0.0825	-0.1835	0.05775	-0.1325
0.0825	0.0475	0.0825	0.1835	0.05775	0.1325	-0.0825	-0.0815	-0.033	-0.2175	0.07425	-0.1325
-0.0825	0.0815	-0.033	0.2175	0.07425	0.1325	-0.066	-0.0815	-0.0165	-0.2175	-0.07425	-0.1665
-0.066	0.0815	-0.0165	0.2175	-0.07425	0.1665	-0.0495	-0.0815	0.	-0.2175	-0.05775	-0.1665
-0.0495	0.0815	0.	0.2175	-0.05775	0.1665	-0.033	-0.0815	0.0165	-0.2175	-0.04125	-0.1665
-0.033	0.0815	0.0165	0.2175	-0.04125	0.1665	-0.0165	-0.0815	0.033	-0.2175	-0.02475	-0.1665
-0.0165	0.0815	0.033	0.2175	-0.02475	0.1665	0.	-0.0815	-0.07425	-0.0305	-0.00825	-0.1665
0.	0.0815	-0.07425	0.0305	-0.00825	0.1665	0.0165	-0.0815	-0.05775	-0.0305	0.00825	-0.1665
0.0165	0.0815	-0.05775	0.0305	0.00825	0.1665	0.033	-0.0815	-0.04125	-0.0305	0.02475	-0.1665
0.033	0.0815	-0.04125	0.0305	0.02475	0.1665	0.0495	-0.0815	-0.02475	-0.0305	0.04125	-0.1665
0.0495	0.0815	-0.02475	0.0305	0.04125	0.1665	0.066	-0.0815	-0.00825	-0.0305	0.05775	-0.1665
0.066	0.0815	-0.00825	0.0305	0.05775	0.1665	0.0825	-0.0815	0.00825	-0.0305	0.07425	-0.1665
0.0825	0.0815	0.00825	0.0305	0.07425	0.1665	-0.0825	-0.1155	0.02475	-0.0305	-0.07425	-0.2005
-0.0825	0.1155	0.02475	0.0305	-0.07425	0.2005	-0.066	-0.1155	0.04125	-0.0305	-0.05775	-0.2005
-0.066	0.1155	0.04125	0.0305	-0.05775	0.2005	-0.0495	-0.1155	0.05775	-0.0305	-0.04125	-0.2005
-0.0495	0.1155	0.05775	0.0305	-0.04125	0.2005	-0.033	-0.1155	0.07425	-0.0305	-0.02475	-0.2005
-0.033	0.1155	0.07425	0.0305	-0.02475	0.2005	-0.0165	-0.1155	-0.07425	-0.0645	-0.00825	-0.2005
-0.0165	0.1155	-0.07425	0.0645	-0.00825	0.2005	0.	-0.1155	-0.05775	-0.0645	0.00825	-0.2005
0.	0.1155	-0.05775	0.0645	0.00825	0.2005	0.0165	-0.1155	-0.04125	-0.0645	0.02475	-0.2005
0.0165	0.1155	-0.04125	0.0645	0.02475	0.2005	0.033	-0.1155	-0.02475	-0.0645	0.04125	-0.2005
0.033	0.1155	-0.02475	0.0645	0.04125	0.2005	0.0495	-0.1155	-0.00825	-0.0645	0.05775	-0.2005
0.0495	0.1155	-0.00825	0.0645	0.05775	0.2005	0.066	-0.1155	0.00825	-0.0645	0.07425	-0.2005
0.066	0.1155	0.00825	0.0645	0.07425	0.2005	0.0825	-0.1155	0.02475	-0.0645		
0.0825	0.1155	0.02475	0.0645	-0.0825	-0.0135	-0.0825	-0.1495	0.04125	-0.0645		

**Table A.4** Description of the fifteen baffles for each neutral beam line. The baffle outlines are given, either as a set of (w,v) coordinates or as a radius. In the case of radius the baffle outline is in a plane parallel to the source grid. The first number in each column is the distance from the source. Dimensions are given in mm.

Component	u	w/radius	V
	1840	0.0	-222
	1840	39.0	-218
	1840	66.0	-208
	1840	81.0	-192
	1840	87.5	-166
	1840	87.5	166
	1840	81.0	192
	1840	66.0	208
Neutraliser II HR	1840	39.0	218
	1840	0.0	222
	1840	-39.0	218
	1840	-66.0	208
	1840	-81.0	192
	1840	-87.5	166
	1840	-87.5	-16
	1840	-81.0	-19
	1840	-66.0	-20
	1840	-39.0	-21
	1840	120.0	-25
200	1840	120.0	250
Magnet entry	1840	-120.0	250
	1840	-120.0	-25
	2260	120.0	-25
Magnet exit	2260	120.0	250
Magnet exit	2260	-120.0	250
	2260	-120.0	-25
Inter-tank duct entry	2799	150.0	_
Inter-tank duct exit	2991	150.0	_
	3171	122.0	-25
Calorimeter element 1	3171	122.0	250
Calorinieter element 1	3171	-125.0	250
	3171	-125.0	-25
	3289	118.0	-25
Calorimeter element 2	3289	118.0	250
Calorimeter element 2	3289	-119.0	250
	3289	-119.0	-25
Duct 1 entry	3851	140.0	_
Duct 1 exit	4080	140.0	
Duct 2 entry	4133	140.0	_
Duct 2 exit	4304	140.0	
Duct 3 entry	4305	158.0	_
Duct 3 exit	4504	158.0	
Duct 4 entry	4575	175.0	_
Duct 4 exit	5142	180.0	_

#### Data availability

Data will be made available on request.

#### References

- R. Koch, Fast particle heating, Fusion Sci. Technol. 57 (02 2010), https://doi.org/ 10.13182/FST10-A9409.
- [2] E.S. Marmar, J.L. Terry, W.L. Rowan, A.J. Wootton, Diagnostic neutral beam and active spectroscopy requirements for the Alcator C-Mod tokamak, Rev. Sci. Instrum. 68 (1) (1997) 265–268, https://doi.org/10.1063/1.1147821, https://pubs.aip.org/ aip/rsi/article-pdf/68/1/265/19052982/265\_1\_online.pdf.
- [3] Y. Luo, W.W. Heidbrink, K.H. Burrell, E. Ruskov, W.M. Solomon, Fast-ion  $D_a$  measurements and simulations in quiet plasmas, Phys. Plasmas 14 (11) (2007) 112503, https://doi.org/10.1063/1.2794320, https://pubs.aip.org/aip/pop/article-pdf/doi/10.1063/1.2794320/14048167/112503\_1\_online.pdf.
- [4] G. Lister, D. Post, R. Goldston, Computer simulation of neutral beam injection into tokamaks using Monte Carlo techniques, in: Proceedings of the 3rd Symposium on Plasma Heating in Toroidal Devices, Varenna, Italy, 1976, p. 303, held in Varenna, Italy
- [5] R. Fowler, J. Holmes, J. Rome, NFREYA -a Monte Carlo beam deposition code for non-circular tokamak plasmas, Report ORNL-TM-6845, Oak Ridge National Laboratory, TN, 1979, https://www.osti.gov/servlets/purl/6088388.
- [6] R. Hawryluk, An empirical approach to tokamak transport, in: B. Coppi, G. Leotta, D. Pfirsch, R. Pozzoli, E. Sindoni (Eds.), Physics of Plasmas Close to Thermonuclear Conditions, Pergamon, 1981, pp. 19–46, https://www.sciencedirect.com/science/ article/pii/B9781483283852500091.
- [7] A. Pankin, D. McCune, R. Andre, G. Bateman, A. Kritz, The tokamak Monte Carlo fast ion module NUBEAM in the national transport code collaboration library, Comput. Phys. Commun. 159 (3) (2004) 157–184, https://doi.org/10.1016/j.cpc.2003.11. 002, https://www.sciencedirect.com/science/article/pii/S0010465504001109.
- [8] M.F.M. De Bock, N.J. Conway, M.J. Walsh, P.G. Carolan, N.C. Hawkes, Ab initio modeling of the motional Stark effect on MAST, Rev. Sci. Instrum. 79 (10) (2008) 10F524, https://doi.org/10.1063/1.2966459, https://pubs.aip.org/aip/rsi/articlepdf/doi/10.1063/1.2966459/15669786/10f524\_1\_online.pdf.
- [9] O. Asunta, J. Govenius, R. Budny, M. Gorelenkova, G. Tardini, T. Kurki-Suonio, A. Salmi, S. Sipilä, Modelling neutral beams in fusion devices: beamlet-based model for fast particle simulations, Comput. Phys. Commun. 188 (2015) 33–46, https://doi.org/10.1016/j.cpc.2014.10.024, https://www.sciencedirect.com/science/article/pii/S0010465514003701.
- [10] B. Geiger, L. Stagner, W. Heidbrink, R. Dux, R. Fischer, Y. Fujiwara, A. Garcia, A.S. Jacobsen, A.J. van Vuuren, A.N. Karpushov, D. Liu, P.A. Schneider, I. Sfiligoi, P.Z. Poloskei, M. Weiland, Progress in modelling fast-ion d-alpha spectra and neutral particle analyzer fluxes using fidasim, Plasma Phys. Control. Fusion 62 (10) (2020) 105008, https://doi.org/10.1088/1361-6587/aba8d7.
- [11] P.M. Stubberfield, M.L. Watkins, Multiple pencil beam, JET DPA(06)87, 1987.
- [12] J. Mandrekas, Physics models and user's guide for the neutral beam module of the SUPERCODE, report GTFR-102, Georgia Institute of Technology, Atlanta, 1992, https://www.osti.gov/servlets/purl/10191990.
- [13] Y. Feng, B. Wolle, K. Hübner, New, simplified technique for calculating particle source rates due to neutral beam injection into tokamaks, Comput. Phys. Commun. 88 (1995) 161–172, https://www.sciencedirect.com/science/article/pii/ 00104655508000136
- [14] M. Schneider, L.-G. Eriksson, I. Jenkins, J. Artaud, V. Basiuk, F. Imbeaux, T. Oikawa, JET-EFDA contributors, ITM-TF contributors, simulation of the neutral beam deposition within integrated tokamak modelling frameworks, Nucl. Fusion 51 (6) (2011) 063019, https://doi.org/10.1088/0029-5515/51/6/063019.
- [15] J. Artaud, V. Basiuk, F. Imbeaux, M. Schneider, J. Garcia, G. Giruzzi, P. Huynh, T. Aniel, F. Albajar, J. Ané, A. Bécoulet, C. Bourdelle, A. Casati, L. Colas, J. Decker, R. Dumont, L. Eriksson, X. Garbet, R. Guirlet, P. Hertout, G. Hoang, W. Houlberg, G. Huysmans, E. Joffrin, S. Kim, F. Köchl, J. Lister, X. Litaudon, P. Maget, R. Masset, B. Pégourié, Y. Peysson, P. Thomas, E. Tsitrone, F. Turco, The cronos suite of codes for integrated tokamak modelling, Nucl. Fusion 50 (4) (2010) 043001, https://doi.org/10.1088/0029-5515/50/4/043001.
- [16] G. Falchetto, D. Coster, R. Coelho, B. Scott, L. Figini, D. Kalupin, E. Nardon, S. Nowak, L. Alves, J. Artaud, V. Basiuk, J.P. Bizarro, C. Boulbe, A. Dinklage, D. Farina, B. Faugeras, J. Ferreira, A. Figueiredo, P. Huynh, F. Imbeaux, I. Ivanova-Stanik, T. Jonsson, H.-J. Klingshirn, C. Konz, A. Kus, N. Marushchenko, G. Pereverzev, M. Owsiak, E. Poli, Y. Peysson, R. Reimer, J. Signoret, O. Sauter, R. Stankiewicz, P. Strand, I. Voitsekhovitch, E. Westerhof, T. Zok, W. Zwingmann, ITM-TF contributors, the ASDEX upgrade team, JET-EFDA contributors, the European integrated tokamak modelling (itm) effort: achievements and first physics results, Nucl. Fusion 54 (4) (2014) 043018, https://doi.org/10.1088/0029-5515/54/4/043018.
- [17] M. Tournianski, Experimental investigation of ion behaviour on the START tokamak, Ph.D. thesis, The University of Essex, 1999, held at https://library.essex.ac. uk/literature/theses.

- [18] S. Bannmann, O. Ford, U. Hoefel, P. Poloskei, A. Pavone, S. Kwak, J. Svensson, S. Lazerson, P. McNeely, N. Rust, D. Hartmann, E. Pasch, G. Fuchert, R. Wolf, The W7-X-team, fast forward modeling of neutral beam injection and halo formation including full balmer-α emission prediction at w7-x, J. Instrum. 18 (10) (2023) P10029, https://doi.org/10.1088/1748-0221/18/10/P10029.
- [19] S. Bannmann, O. Ford, U. Hoefel, P.Z. Poloskei, A. Pavone, S. Kwak, J. Svensson, S. Lazerson, P. McNeely, N. Rust, D. Hartmann, E. Pasch, G. Fuchert, A. Langenberg, N. Pablant, K.J. Brunner, R.C. Wolf, The W7-X team, Bayesian inference of electron density and ion temperature profiles from neutral beam and halo balmer-α emission at wendelstein 7-x, Plasma Phys. Control. Fusion 66 (6) (2024) 065001, https://doi.org/10.1088/1361-6587/ad3c1d.
- [20] D.A. Homfray, D. Ciric, V. Dunkley, R. King, D. Payne, M.R. Simmonds, B. Stevens, P. Stevenson, C. Tame, S.E.V. Warder, A.M. Whitehead, D. Young, Overview of MAST neutral beam system performance, in: 2009 23rd IEEE/NPSS Symposium on Fusion Engineering, 2009, pp. 1–4, https://doi.org/10.1109/FUSION.2009.5226423.
- [21] A. Holmes, R. McAdams, Space charge compensation of positive ion beams used in magnetic fusion applications, Nucl. Fusion 62 (6) (2022) 066017, https://doi.org/ 10.1088/1741-4326/ac544c.
- [22] P. Veltri, E. Sartori, P. Agostinetti, D. Aprile, M. Brombin, G. Chitarin, N. Fonnesu, K. Ikeda, M. Kisaki, H. Nakano, A. Pimazzoni, K. Tsumori, G. Serianni, Ion beam transport: modelling and experimental measurements on a large negative ion source in view of the ITER heating neutral beam, Nucl. Fusion 57 (1) (2016) 016025, https://doi.org/10.1088/0029-5515/57/1/016025.
- [23] E. Surrey, C. Challis, D. Ciric, S. Cox, B. Crowley, I. Jenkins, T. Jones, D. Keeling, Measurement of the depletion of neutraliser target due to gas heating in the JET neutral beam injection system, Fusion Eng. Des. 73 (2) (2005) 141–153, https://doi.org/ 10.1016/j.fusengdes.2005.06.348, https://www.sciencedirect.com/science/article/ pii/S0920379605003832.
- [24] D.B. King, C.D. Challis, E.G. Delabie, D. Keeling, G.F. Matthews, A. Shepherd, S. Silburn, JET contributors, Neutral beam injection on JET: effect on neutron discrepancy and energy balance, in: 45th EPS Conference on Plasma Physics, vol. 352, Prague, 2018, paper number: P4.1067, available as a downloadable report, https://scientific-publications.ukaea.uk/wp-content/uploads/UKAEA-CCFE-CP1801.pdf.
- [25] D. King, R. Sharma, C. Challis, A. Bleasdale, E. Delabie, D. Douai, D. Keeling, E. Lerche, M. Lennholm, J. Mailloux, G. Matthews, M. Nicassio, Ž. Štancar, T. Wilson, J.E.T. Contributors, Tritium neutral beam injection on JET: calibration and plasma measurements of stored energy, Nucl. Fusion 63 (11) (2023) 112005, https://doi.org/10.1088/1741-4326/acce97.
- [26] D. Ciric, J. Milnes, E. Surrey, Influence of accelerator grid misalignment on multiaperture particle beam properties, in: Proceedings of the 19th IEEE/IPSS Symposium on Fusion Engineering. 19th SOFE (Cat. No.02CH37231), 2002, pp. 56–59, https:// doi.org/10.1109/FUSION.2002.1027641.
- [27] D. Ciric, H.D. Falter, D.J. Godden, Space and time resolved doppler spectroscopy of neutral beams, in: B. Beaumont, P. Libeyre, B. de Gentile, G. Tonon (Eds.), Proceedings of the 20th Symposium on Fusion Technology (SOFT 1998), Association Euratom-CEA Cadarache, Saint-Paul-Lez-Durance, France, 1999, pp. 469–472, published in Fusion Technology 1998, https://scipub.euro-fusion.org/wp-content/ uploads/2014/11/JETC98040.pdf.
- [28] D. Godden, Plasma non-uniformity in the JET neutral beam injection source measurement, simulations and development of an improved source, Ph.D. thesis, Dublin City University, 2000. https://doras.dcu.je/18755/1/Daniel J Godden.pdf.
- [29] D.J. Godden, D. Ciric, H.D. Falter, Modelling ion source uniformity, in: Proceedings of the 21st Symposium on Fusion Technology (SOFT), Madrid, Spain, 2000, Available as a downloadable report: https://scipub.euro-fusion.org/wp-content/uploads/ 2014/11/EFDC00111.pdf. (Accessed 20 January 2025).
- [30] G. Duesing, H. Altmann, H. Falter, A. Goede, R. Haange, R.S. Hemsworth, P. Kupschus, D. Stork, E. Thompson, Neutral beam injection system, Fusion Technol. 11 (1) (1987) 163–202, https://doi.org/10.13182/FST87-A25004.
- [31] T. Barrett, Neutral beam physics and beamline position parameters, Design Process CD/MU/00038, UK Atomic Energy Authority, updated: 19th July 2012 (July 2012).
- [32] J. Svensson, A. Werner, Large scale bayesian data analysis for nuclear fusion experiments, in: 2007 IEEE International Symposium on Intelligent Signal Processing, 2007, pp. 1–6, https://doi.org/10.1109/WISP.2007.4447579.
- [33] S.D. Pinches, J.-F. Artaud, F.J. Casson, Progress in the ITER integrated modelling programme and the ITER scenario database, in: Proceedings of the 27th IAEA Fusion Energy Conference (FEC 2018), International Atomic Energy Agency (IAEA), IAEA-CN-258, Ahmedabad, India, 2018, p. 504.
- [34] ITER organisation, Contains publicly accessible ITER repositories on github, https://github.com/iterorganization, 2025. (Accessed 20 January 2025).
- [35] T.R. Barrett, C. Jones, P. Blatchford, B. Smith, R. McAdams, N. Woods, Engineering design of the double neutral beam injection system for MAST upgrade, in: Proceedings of the 26th Symposium of Fusion Technology (SOFT-26), Fusion Eng. Des. 86 (6) (2011) 789–792, https://doi.org/10.1016/j.fusengdes.2011.01.020, https://www.sciencedirect.com/science/article/pii/S0920379611000329.